Catalysis Science & Technology

ROYAL SOCIETY OF CHEMISTRY

PAPER

Cite this: *Catal. Sci. Technol.*, 2025, **15**, 5907

Enhanced ethanol reforming with catalytic active ruthenium species derived from solid solution in lanthanum chromite

Tamara S. Moraes, †[a] Victor B. Tinti, †[bc] Daniel Z. de Florio, [b] Andre S. Ferlauto, [b] Fernando Piazzolla,[a] Yohei Miura,[d] David P. Dean,[e] Hien N. Pham,[f] Jeffrey T. Miller,[e] Abhaya K. Datye [f] and Fabio C. Fonseca *[a]

Ethanol steam reforming (ESR) is a promising route for renewable hydrogen production, but it requires highly active and coke resistant catalysts to efficiently convert ethanol into hydrogen-rich mixtures. The ESR catalytic activity is investigated in single-phase $LaCr_{1-x}Ru_xO_3$ solid solutions with $0.0 \leq x \leq 0.20$. Highly active ruthenium species are formed at the surface of the oxide *in operando* during ESR at 600 °C. These species have remarkable stability for ESR with strong resistance for coke formation, resembling single-atom catalysts. Samples reduced *ex situ* at higher temperature (900 °C) exhibit Ru exsolved nanoparticles with lower catalytic stability than the species obtained *in operando* during ESR reaction. X-ray absorption spectroscopy and high-resolution transmission electron microscopy reveal that small metallic Ru species (≤2 nm) are formed under ESR reaction, whereas in samples exsolved at 900 °C such species coexist with larger exsolved Ru particles (~5 nm), which are more likely to deactivate. The experimental results provide an innovative approach for solid solution-derived species in refractory oxide matrix that are valuable for designing robust catalysts for ESR.

Received 25th June 2025,
Accepted 19th August 2025

DOI: 10.1039/d5cy00774g

rsc.li/catalysis

1. Introduction

Recently, ethanol derived from biomass has emerged as an attractive hydrogen carrier due to its renewable origin and energy efficiency.[1–3] This biofuel offers simplified storage and transportation, as well as the potential to produce hydrogen *via* the ethanol steam reforming (ESR) reaction.[4,5] Compared to methane, ethanol provides safer and denser energy storage owing to its liquid state under ambient conditions.[6,7] This characteristic is particularly advantageous for mobile applications, such as trucks and cars, where storage space is limited but autonomy is critical. Furthermore, ethanol can seamlessly integrate with existing liquid fuel infrastructures, such as gasoline and diesel distribution networks. As a result, ethanol has become the most widely used biofuel in combustion engines across several countries.

Ethanol steam reforming (ESR) (eqn (1)) involves multiple chemical pathways, with several parallel reactions occurring depending on the catalyst and reaction conditions.[3]

$$C_2H_5OH + H_2O \rightarrow 2CO + 4H_2 \quad (1)$$

These reactions typically convert ethanol into various products. The main reactions include:

i) **Ethanol dehydrogenation**, which produces acetaldehyde (C_2H_4O) and hydrogen gas (H_2) (eqn (2)).

$$C_2H_5OH \rightarrow C_2H_4O + H_2 \quad (2)$$

ii) **Ethanol dehydration**, forming ethylene (C_2H_4) and water (H_2O) (eqn (3)).

$$C_2H_5OH \rightarrow C_2H_4 + H_2O \quad (3)$$

[a] *Nuclear and Energy Research Institute, IPEN-CNEN, São Paulo, 05508-000, Brazil. E-mail: fabiocf@usp.br*
[b] *Center for Engineering, Modeling and Applied Social Sciences, Federal University of ABC, Santo André 09210-580, SP, Brazil*
[c] *Department of Energy Conversion and Storage, Technical University of Denmark, 2800 Kgs. Lyngby, Denmark*
[d] *Nissan Research Centre, Nissan Motor Corporation Limited, Kanagawa, 237-8523, Japan*
[e] *Davidson School of Chemical Engineering, Purdue University, 480 Stadium Mall Drive, West Lafayette, IN 47907-2100, USA*
[f] *Department of Chemical & Biological Engineering and Center for Micro Engineered Materials, University of New Mexico, Albuquerque, NM, 87131, USA*
† These authors contributed equally to the work.

iii) **Ethanol decomposition**, yielding methane (CH_4), hydrogen gas (H_2), and carbon monoxide (CO) (eqn (4)).

$$C_2H_5OH \rightarrow CH_4 + H_2 + CO \quad (4)$$

iv) **Methane steam reforming (MSR)**, which generates CO and H_2 (eqn (5)).

$$CH_4 + H_2O \rightarrow CO + 3H_2 \quad (5)$$

v) **Water–gas shift reaction (WGSR)**, where CO from the preceding reactions reacts with water to produce carbon dioxide (CO_2) and additional hydrogen gas (H_2) (eqn (6)).

$$CO + H_2O \rightarrow CO_2 + H_2 \quad (6)$$

Under certain conditions, solid carbon deposits (coke) can form as a byproduct of ethanol decomposition or its intermediates.[8] This is generally an undesirable side reaction. Factors influencing coke formation include temperature, pressure, catalyst type (*e.g.*, nickel-based catalysts), and reactor residence time. Optimizing reaction conditions and catalyst selection is crucial for maximizing the yield of desired products, such as hydrogen gas.

Lanthanum chromite ($LaCrO_3$) is a p-type electronic conductor known for its high stability in both reducing and oxidizing atmospheres. These properties make it one of the preferred materials for applications such as interconnectors in high-temperature solid oxide fuel cells (SOFCs).[9–12] A key challenge in using $LaCrO_3$ in SOFCs lies in achieving a dense ceramic due to its limited sintering characteristics.[12] Nonetheless, its resistance to densification, combined with its stability across a wide range of temperatures and oxygen partial pressures, makes $LaCrO_3$-based ceramics ideal for high-temperature catalytic applications. In such applications, the stability and durability of the substrate supporting catalytic active sites are critical to maintaining high performance, preserving morphology, and avoiding grain coarsening. Additionally, perovskite-based materials are promising for catalysis due to their resistance to coke deposition and weak binding to sulfur.[13,14]

The ABO_3 perovskite structure is highly versatile, allowing for high concentration doping at the B-site. The hybridization of orbitals and charge transfer between the transition metal at the B-site and oxygen are typically identified as mechanisms governing their electronic, magnetic, and catalytic properties.[15] Ruthenium-doped lanthanum chromite ceramics have demonstrated excellent catalytic performance for methane and heavy hydrocarbon reforming. Previous research has shown that materials doped or impregnated with Ru are effective catalysts for methane reforming,[16,17] and that Ru is an active catalyst for ESR.[17–19] Moreover, Ru-substituted $LaCrO_3$ has been studied as an effective catalyst for various reactions,[20–25] but only recently our group reported its use for ESR.[26] In impregnated catalysts, highly dispersed Ru nanoparticles derived from cluster precursors were significantly smaller than those produced from metal-salt precursors.[17,18] These catalysts outperformed those prepared using conventional impregnation methods with inorganic salts.

More recently, ruthenium species in doped $LaCrO_3$ have been shown to exhibit distinct catalytic properties depending on their origin, either as segregated oxide particles or as exsolved nanoparticles. Exsolution involves the formation of metallic particles from ionic species in a solid solution, typically within a mixed-oxide ceramic phase, through thermochemical treatment under reducing conditions.[27,28] The resulting nanoparticles are nanometric and resistant to agglomeration due to their strong substrate bond. This resistance arises because nucleation begins just below the substrate surface, leaving the exsolved particles partially embedded in the oxide matrix.[29–31]

Recent studies have explored the role of exsolved metals from perovskites in ESR reactions.[32,33] For example, in perovskite titanates such as $(La_{0.5}Ca_{0.5})_{(1-\alpha)}Ni_{0.06}Ti_{0.94}O_{3-\delta}$, A-site deficiency has been shown to influence the size and abundance of exsolved nickel particles.[23,33] These nickel nanoparticles exhibited significant catalytic activity in ESR reactions, achieving complete ethanol conversion at 750 °C. However, controlling and maintaining the nanoparticle size at a few nanometers remains a challenge.

A similar approach to achieving highly dispersed active sites has been explored in other catalyst systems, where a dopant active metal ion is dissolved in the oxide matrix.[34] Maintaining a low dopant concentration prevents phase segregation and ensures a solid solution. This method has been extensively studied for preparing single-atom catalysts derived from metal ionic species in solid solutions within an oxide matrix. For instance, a recent study investigated various synthesis methods for Ni-doped ceria.[35] Depending on the catalyst preparation method, high-resolution electron microscopy revealed nickel species in different forms: large NiO particles on the ceria surface, small NiO ensembles, or nickel ions incorporated into the ceria lattice. The most active species for acetylene hydrogenation were nickel ions integrated into the lattice, whereas Ni-impregnated samples showed poor performance.

A more recent study on metal-support interactions in Ru-doped $LaCrO_3$ observed that Ru species emerged on the perovskite surface in various forms, including 3D nanoparticles, 2D layers, and 0D single atoms.[21]

The present study demonstrates a novel strategy for achieving high catalytic activity in ethanol steam reform using ruthenium substituted $LaCr_{1-x}Ru_xO_3$ compounds. Under reaction conditions, small metallic Ru species are generated resulting in enhanced catalytic activity as compared to catalysts prepared either by exsolution or by standard impregnation. Combined with the stable $LaCrO_3$ matrix, the solid-solution-derived Ru species provide a robust catalyst for hydrogen production from an economically viable renewable carrier.

2. Experimental

2.1. Catalyst preparation

Ceramic powders of Ru-doped lanthanum chromite $La(Cr_{1-x}Ru_x)O_3$, x = 0, 0.05, 0.10, and 0.20, were produced by the Pechini method.[36,37] $La(NO_3)_3{\cdot}6H_2O$ (99.9% Sigma Aldrich), $Cr(NO_3)_3{\cdot}9H_2O$ (99.9%, Sigma Aldrich), and $RuCl_3{\cdot}nH_2O$ (99.9%, Sigma Aldrich) were the cation precursors. Citric acid was employed as a chelation agent, and ethylene glycol for polyesterification. A molar ratio of 1 : 2 : 4 of metallic ions : citric acid : ethylene glycol was adopted. First, the citric acid and ionic precursors were solubilized in water and kept under stirring for two hours to ensure full solubilization and homogenization. Following, the ethylene glycol was added, and the solution was heated to 180 °C to eliminate excess water and induce the polymerization of the chelates. A dark and brittle metal–organic resin was produced, which then was ground into a fine powder. The resin was calcined in air at 1000 °C for 1 hour in air to eliminate organics and crystallize the ceramic material. For the sake of simplicity, the compositions with Ru x = 0, 0.05, 0.10, and 0.20 are referred to as LCR0, LCR5 (2.1 wt% Ru), LCR10 (4.1 wt% Ru), and LCR20 (8.1 wt% Ru), respectively.

The formation of active solid-solution derived Ru species was done *in operando* during ESR reactions. The effect of exsolution was further investigated by *ex situ* reduction heat treatment under hydrogen flow. The *ex situ* thermochemical heat treatment of the as-prepared powders were carried out by following one of the two procedures: i) at 900 °C for 4 hours under pure H_2 (99.999%) flow (100 sccm) in a tubular furnace with controlled atmosphere, referred to as LCR*x*-exs samples, or ii) at 250 °C or 550 °C, in the fixed-bed catalytic test furnace reactor or in the X-ray absorption spectroscopy sample holder, as described next. The *ex situ* exsolution treatments were performed by flowing H_2 at the targeted temperature, while both heating and cooling down to room temperature ramps were under inert gas flow.

A reference impregnated sample (LCR-imp) was obtained by adding a solution of $RuCl_3$ into the LCR0 with ~10% molar (4.0 wt%) Ru doping. The impregnated powder was calcined at 700 °C in air.

2.2. Catalyst characterization

X-ray diffraction (XRD) was used to identify the crystalline phases. The XRD was measured in a STADI-P X-ray powder diffractometer (STOE). The samples were placed in the middle of two cellulose acetate foils and measured in transmission geometry. Data were collected in a range from 5° to 50° (2θ) with an angular step of 0.015°. The radiation of $MoK_{\alpha1}$ (0.7093 Å) was filtered by a primary beam monochromator (Ge (111) crystal). The diffraction results were fitted using Rietveld refinement and the TOPAS software to obtain quantitative information about the crystal structure.[38,39]

Temperature-programmed reaction (TPR) experiments were performed in a TPR/TPD 2900 Micromeritics system equipped with a thermal conductivity detector (TCD). The catalyst was dried under a helium (He) flow (30 mL min^{-1}), and the analysis was carried out under a flow of a gas mixture of 5% H_2/Ar (30 mL min^{-1}), using 100 mg of sample. The temperature was increased to 1000 °C at a heating rate of 10 °C min^{-1}.

Analysis of the chemical composition of the catalysts was performed by X-ray fluorescence spectroscopy (WDXRF) using the Rigaku Supermini200, with an X-ray tube of 50 kV, 200 W (Pd-anode).

Raman spectra were carried out to identify both changes in the perovskite lattice by the addition of ruthenium and to evaluate coke formation after ESR reactions. The catalysts were analyzed in a Raman Horiba Jobin Yvon/XploRA PLUS Spectrometer, model 800 equipped with LabRAM confocal microscope Olympus BX40 Model coupled to a HORIBA Instruments Incorporated/SyncerityTM CCD Detector using a He–Ne laser ions (λ = 632 nm).

Scanning electron microscopy (SEM) was used to characterize the morphology of the powder. High-magnification images were obtained on a JEOL microscope (model JMS-6701F) with a field emission gun (FEG-SEM). Energy dispersive X-ray spectroscopy (EDS) analyses were performed to verify the stoichiometry of the produced powders, using a JEOL JSM-6010LA microscope.

Transmission electron microscopy (TEM) was employed to verify local crystal structure and sample morphology. The analyses were performed on a JEOL JEM-2010 microscope. Samples were prepared by depositing a suspension of the catalysts in isopropyl alcohol onto a 200 mesh copper grid coated with Formvar and carbon (Ted Pella, Inc.). The samples were air-dried for 24 hours. To obtain atomic-scale images and EDS mapping we used an aberration-corrected STEM JEOL 200 CF NeoArm equipped with dual EDS detectors (ACSTEM-EDS). Both bright field and annular dark field images were recorded.

X-ray photoelectron spectroscopy (XPS) was performed by using a Phi 5000 VersaProbe II X-ray photoelectron spectrometer at Nissan Research Center (Japan). For XPS measurements the energy scale is calibrated by using the binding energy for an La $4d_{5/2}$ peak top, 101.7 eV.

Ru K edge X-ray absorption spectroscopy (XAS) was conducted at the Argonne National Laboratory Advanced Photon Source 10-BM MRCAT bending magnet beam line. Samples were pressed into separate sample holders, which were all sealed inside an *in situ* gas/temperature treatment cell with X-ray transparent windows. Three ion chambers were used, which enables simultaneous measurement of the Ru foil, used for an extended X-ray absorption fine structure, EXAFS, (12 Ru-Ru at 2.68 Å) reference. The samples were scanned over an energy range from 250 eV to 1 keV above the edge. The X-ray absorption near-edge structure (XANES) spectra were normalized with a linear and cubic fit of the pre-edge and post-edge regions, respectively. All spectra were calibrated to Ru foil (22.1172 keV), which was acquired at the same time as the samples. A 2% Ru/SiO_2 sample was used as

a reference XANES spectrum for metallic Ru NPs. The sample was synthesized using incipient wetness impregnation (IWI). Davisil grade 646 silica (35–60 mesh, Sigma-Aldrich) was used as a support. 2 wt% Ru, from a ruthenium(III) acetylacetonate precursor, was dissolved in acetone and deposited on the silica dropwise while mixing. The sample was dried for 6 hours at room temperature, then overnight at 125 °C. The sample was calcined at 300 °C in air for 3 hours, cooled to room temperature, then reduced at 550 °C in 5% H_2 for 3 hours.

The samples LCR*x*, LCR*x*-exs, LCR-imp, and Ru/SiO_2 were scanned as-received in He flow at 25 °C. Exposure to air at RT leads to surface oxidation of Ru NPs. The samples were then heated to 550 °C in 3% H_2 in balance He for 30 minutes and scanned again. After this scan, the samples were cooled to 25 °C in 3% H_2 in balance He and scanned. Finally, 20% O_2/He was flowed for 30 minutes and scanned one more time. This final low-temperature oxidation leads to surface oxidation of the Ru NPs present in the sample.

2.3. ESR

Ethanol steam reforming was performed at atmospheric pressure in a fixed bed reactor at 600 and 700 °C using 5, 10, 20, or 50 mg of catalysts. The reactive feed consisted of 2.5 vol% ethanol and 7.5 vol% water, diluted in the N_2 carrier stream. The reactant mixture was obtained by flowing N_2 streams through two saturators containing ethanol and water separately (30 and 30 mL min^{-1}, respectively), which were maintained at 18 °C and 54 °C, respectively, to obtain the desired H_2O/ethanol molar ratio of 3/1. The reactants and the reaction products were analyzed by gas chromatography (Agilent 7890A), equipped with a thermal conductivity detector (TCD) and a flame ionization detector (FID) connected in series and two columns (molecular sieve and PLOT U). Ethanol conversion ($X_{ethanol}$) (eqn (7)) and product distribution (S_x) (eqn (8)) were determined as follows:

$$X_{ethanol} = \frac{(n_{ethanol})in - (n_{ethanol})out}{(n_{ethanol})in} \times 100 \quad (7)$$

$$S_x = \frac{(n_x)\ produced}{(n_t)\ produced} \times 100 \quad (8)$$

where (n_x) produced = moles of x produced (x = reaction products) and (n_t) produced = sum of the moles of products (excluding water).

The ESR test protocol proceeded as follows: first, the catalyst powder was loaded into a quartz tube between quartz wool plugs. Starting from room temperature the furnace was heated at a rate of 10 °C min^{-1} under N_2 flow. Once the desired reaction temperature (typically 600 °C) was reached, the system was allowed to stabilize for 90 minutes while the N_2 flow began to flow into the saturators to prepare the mixture of H_2O/ethanol with a molar ratio of 3/1. After temperature stabilization, the reactant mixture was flown through the quartz tube, and the outlet was subsequently analyzed by gas chromatography (GC). In the present study, unless otherwise stated, the ESR tests were conducted without pre-reduction treatment of the samples. Gas sampling during ESR tests at fixed temperature intervals occurred every 34 minutes. After the ESR tests, samples were cooled under nitrogen to preserve the spent catalysts for post-test analyses. Regeneration tests under a water-rich atmosphere or nitrogen were performed by discontinuing the ethanol flow in the reactor.

3. Results and discussion

3.1. Ethanol steam reforming performance

Ethanol conversion and product distribution as a function of time on stream (TOS) for the ESR at 600 °C are shown in Fig. 1. It is worth mentioning that the as-prepared samples were tested following the protocol described in the Experimental section without any pre-treatment before the ESR reaction.

The most notable result is the high catalytic activity of the oxide compounds LCR10 and LCR20 for ESR, achieving 100% ethanol conversion and maintaining high stability over 20 hours (Fig. 1c and d). The parent compound (LCR0) was inactive for the ESR reaction (Fig. 1a). The main reaction taking place was ethanol dehydrogenation, forming acetaldehyde (C_2H_4O) and H_2.[40] Ethanol can undergo dehydration to produce acetylene, which in turn can decompose into coke and hydrogen, possibly accounting for the deactivation observed within the first hours of the reaction, whereas the LCR5 catalyst initially facilitated ESR and WGS reactions, producing H_2, CO, and CO_2 during the first 2 hours. However, after this period, its activity declined, leading to a shift in selectivity toward acetaldehyde, which stabilized as the predominant product for the remaining 18 hours (Fig. 1b).

On the other hand, Ru doping levels of $x \geq 0.1$ resulted in highly active LCR samples. For these samples, the primary products were H_2, CO, and CO_2, derived from the ethanol steam reforming and water–gas shift reactions. Notably, the LCR10 sample exhibited exceptional ESR performance, with 100% ethanol conversion and no signs of deactivation after 20 hours.

Fig. 1a–d shows the effect of Ru substitution on the catalytic properties of the $LaCrO_3$ perovskite matrix. The ESR is only active when Ru substitution is $x \geq 10\%$, whereas the $LaCrO_3$ parent compound and catalysts with lower amounts of substituted Ru have poor activity for ESR. Such a behavior indicates that, when Ru amount is $x < 10\%$, the dehydrogenation promoted by the oxide matrix prevails. In catalysts with higher fractions of Ru, enough active species are produced that can sustain the ESR.

Raman spectroscopy (Fig. 1e) was utilized to investigate catalyst deactivation. It provides insights into the decline in ethanol conversion observed during the initial hours of reaction for LCR0 and LCR5. The spectra of the spent catalysts revealed two distinct bands: one at 1315 cm^{-1} and

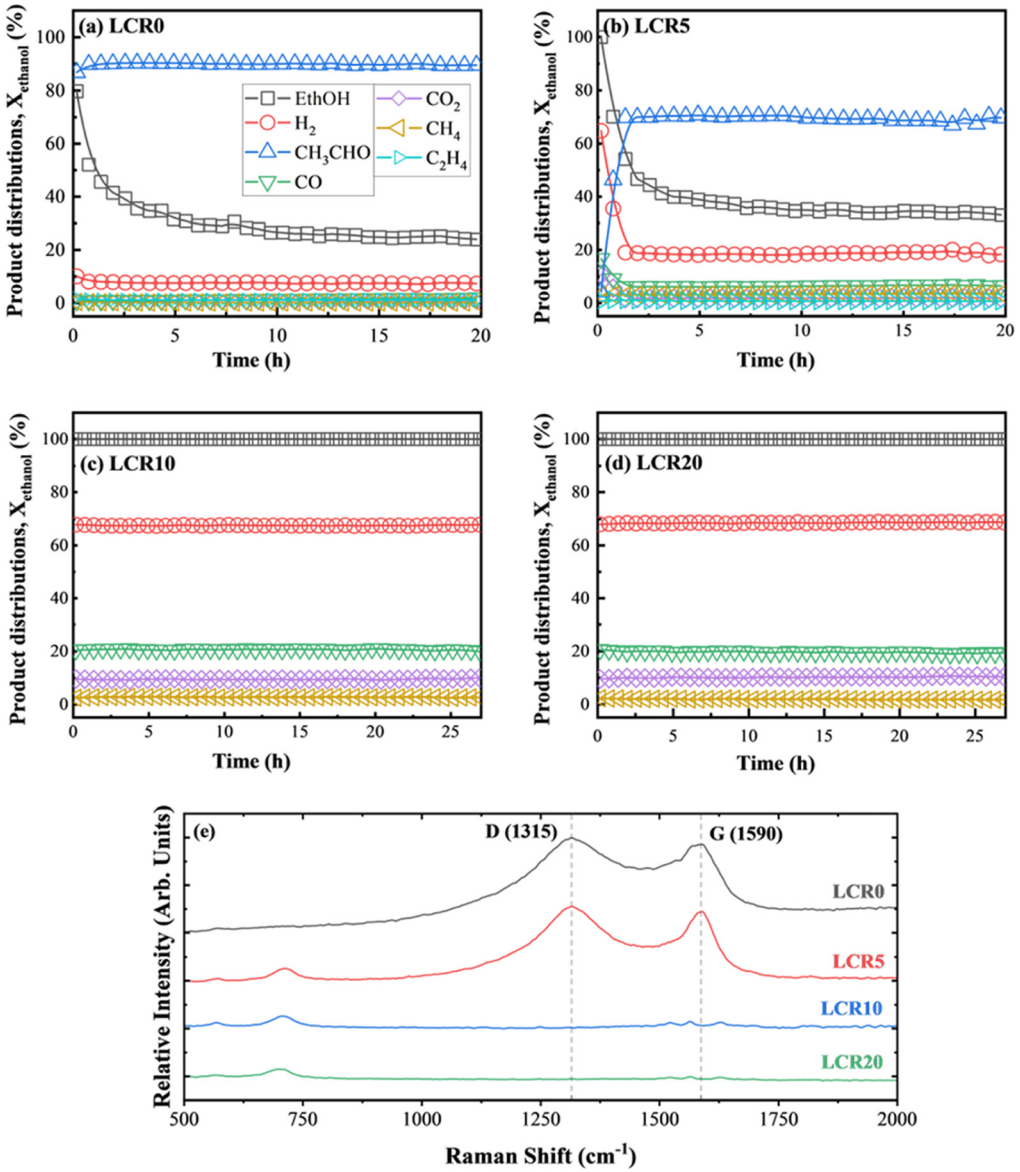

Fig. 1 Composition impact on catalysis. Ethanol conversion over time. Ethanol conversion (□ $X_{ethanol}$) and product distributions *versus* TOS for ESR at 600 °C under H_2O/ethanol molar ratio = 3.0 for samples $LaCr_{1-x}Ru_xO_{3-\delta}$ (a) x = 0 LCR0, (b) x = 0.05 LCR5, (c) x = 0.10 LCR10, and (d) x = 0.20 LCR20 (mass of catalyst = 50 mg and residence time = 0.075 g s mL^{-1}). e) Raman spectra of spent catalyst after ESR.

another at 1590 cm^{-1}, corresponding to the D and G bands of sp^2 carbon, respectively. These prominent carbon bands confirm coke deposition on the material surface during the ESR reaction.[41,42] In contrast, the Raman spectra of the spent LCR10 and LCR20 catalysts did not show the D and G bands after the reaction. The absence of these carbon-related bands indicates that these catalysts are resistant to carbon deposition. Furthermore, sintering of the active species is unlikely due to the relatively low ESR reaction temperature compared to the catalyst fabrication temperatures (1000 °C).

Minor bands observed at ~480 and ~700 cm^{-1} are attributed to vibrational modes of the perovskite matrix and do not relate to carbon species. In particular, the peak near 700 cm^{-1} corresponds to the B_{2g} vibrational mode of the $LaCrO_3$ orthorhombic structure (*Pbnm* symmetry), as reported in previous Raman studies of chromite perovskites.[43] These bands further confirm the chromite structure of the catalyst surface and are not indicative of deactivation or reaction byproducts.

Thermogravimetric analysis and differential thermal analysis (TGA/DTA) measurements (Fig. S1) were also conducted on the spent catalysts to detect the presence of carbon deposits. Measured mass losses of the spent catalyst were close to the detection limit (~5%) of the experimental apparatus. For the LCR5 samples, which experienced significant deactivation, a characteristic exothermic event was observed around 300 °C, accompanied by a slight mass loss. These features are indicative of the inhibited carbon accumulation on the surface of the spent catalyst.

Interestingly, additional ESR tests carried out with samples reduced *ex situ* by thermal treatments at 900 °C in H_2 (LCR*x*-exs) show a decreased performance when compared to the as-prepared samples performance (Fig. S2).

3.2. Catalyst stability and regeneration

To further investigate the active ruthenium species, the stability of the catalysts was evaluated over extended periods (>100 hours). These tests were conducted by reducing the residence time to achieve lower conversion rates, enabling a detailed analysis of catalyst deactivation, as shown in Fig. 2. Additional measurements show the catalytic properties of the sample reduced *ex situ* at 900 °C (LCR20-exs) in Fig. S3.

For ESR tests conducted at 600 °C (Fig. 2a), the LCR20 sample maintained 100% ethanol conversion for approximately 85 hours of operation, demonstrating superior performance of the catalytic active species derived from the solid solution without requiring any previous reduction treatment. The catalytic activity facilitated the conversion of ethanol into H_2, CO, CO_2, and trace amounts of CH_4.

In contrast, Ru-impregnated reference sample (LCR-imp) exhibited a more pronounced degradation compared to the LCR20 catalyst (Fig. 2b). Unlike LCR20, the impregnated sample showed continuous deactivation during the initial hours of the reaction.

Deactivation was marked by a slight decline in H_2 and CO production, accompanied by an increase in acetaldehyde formation. Additional catalytic tests were performed to further explore the LCR properties. Adding excess water to ESR was ineffective in preventing sample deactivation (Fig. S4).

It is worth noting that in Fig. 2a, the LCR20 catalyst exhibits an abrupt decrease in ethanol conversion at ~80 hours and 300 hours of TOS. These sharp drops in activity may indicate the onset of catalyst deactivation events such as the accumulation of surface carbon species, pore blockage, or restructuring of surface Ru active sites. While the catalyst maintains high stability for extended periods, these deactivation events suggest that under prolonged operation, the balance between coke formation and gasification may become unstable promoting stepwise deactivation of the catalyst.

During stability tests, ethanol/steam injection was paused for 2 hours, leaving the catalysts under an N_2 flow at 600 °C. Upon reinjection of the ESR reaction mixture, both the LCR20 and reference LCR-imp catalysts restored 100% ethanol conversion and selectivity, matching their initial

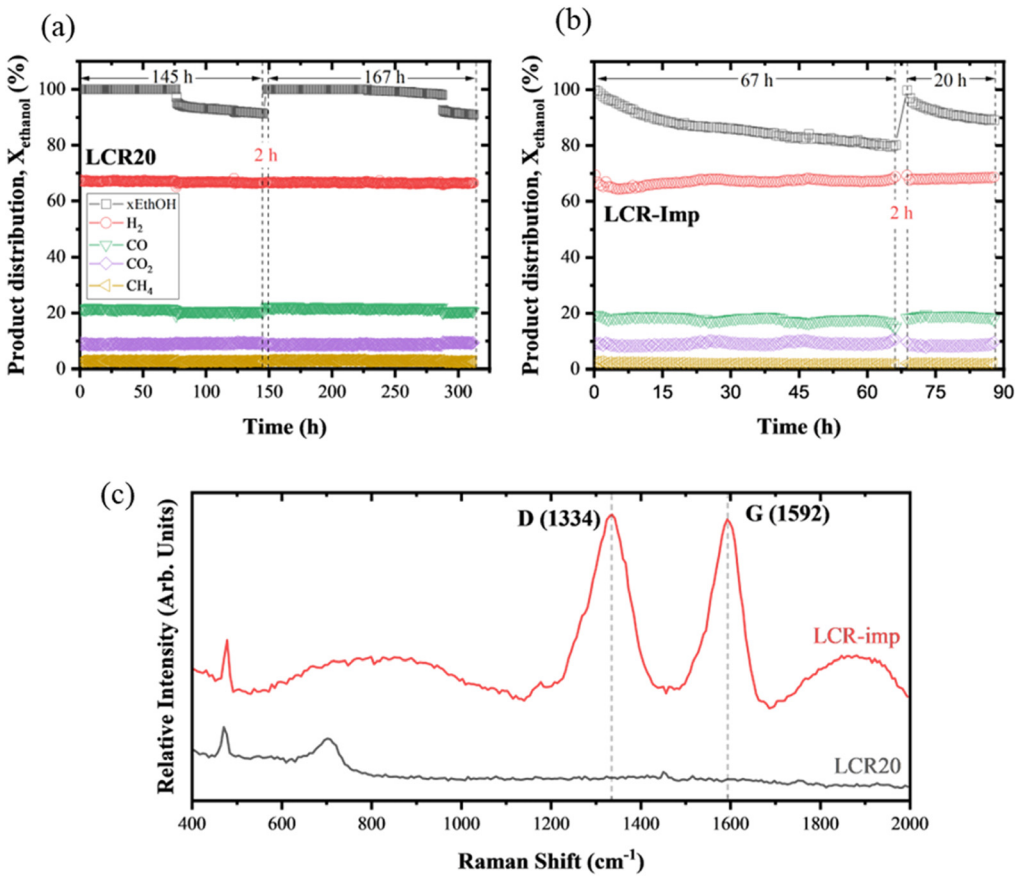

Fig. 2 Endurance catalytic testing. Ethanol conversion (□, $X_{ethanol}$) *versus* TOS for ESR at 600 °C under H_2O/ethanol molar ratio = 3.0 over LCR20 (a) and LCR-imp (b) catalysts (mass of catalyst = 20 mg and residence time = 0.020 g s mL^{-1}). The time interval for regeneration under N_2 was 2 hours. (c) Raman spectra of used catalysts after reactions.

performance. These results indicate that both catalysts can be regenerated by brief exposure to an inert gas at the same temperature as the ESR reaction.

The catalysts used in the stability tests were analyzed by Raman spectroscopy after the reaction. Only the LCR-imp catalyst exhibited the presence of D and G bands, which are characteristic of carbon deposition on the catalyst surface. The recovery of catalytic activity in the LCR-imp catalyst can be attributed to the presence of oxidizing species adsorbed on the catalyst surface, such as CO_2, along with oxygen from the perovskite lattice.[44,45] These species assist in the removal of coke deposited on the catalyst surface. In contrast, the regeneration of the LCR20 catalysts may be attributed to the desorption of weakly bound species from the catalyst surface, which hinder access to active sites.

3.3. Effect of reduction temperature

The catalytic properties of LCR samples towards ESR reactions were further investigated using the LCR10 catalyst and decreasing the residence time relative to the initial tests (Fig. 1 and S2) to avoid complete conversion. Three different tests were performed, each using fresh samples of the LCR10 catalyst subjected to different (*ex situ*) reducing treatments under H_2 in the catalytic test reactor before ESR tests. In the first test, the ESR reaction was carried out without reduction (Fig. 3a) of the catalyst, similar to the tests shown in Fig. 1. The second test was carried out after reduction at 250 °C for 1 hour in H_2 before the reaction (Fig. 3b). The effect of increasing the reducing temperature was investigated in a sample reduced at 550 °C for 1 hour in H_2 prior to the ESR reaction (Fig. 3c). Such temperatures were defined after TPR runs of the LCR samples (Fig. 4).

The test performed with as-prepared LCR10 sample showed an initial conversion of ~80%, which gradually decreased to 50% within 10 hours of reaction. The main products were H_2, CO, CO_2, and acetaldehyde (C_2H_4O). These results suggest that the ESR reaction is the dominant process, but as the catalyst deactivates, ethanol dehydrogenation becomes prevalent. The ESR test following reduction at 250 °C showed slightly better initial activity than the non-reduced test, achieving 100% conversion that rapidly decreased to 60%, with stabilization up to 15 hours. Product selectivity remained similar in both tests, with acetaldehyde increasing and CO decreasing as the reaction proceeded. In contrast, the sample reduced at 550 °C reached 100% conversion with slower deactivation, dropping to 80% conversion after 15 hours. The primary products were H_2, CO, and CO_2, with acetaldehyde increasing as the reaction deactivated.

The combined catalytic tests revealed that the LCR samples are activated *in operando* by the reducing

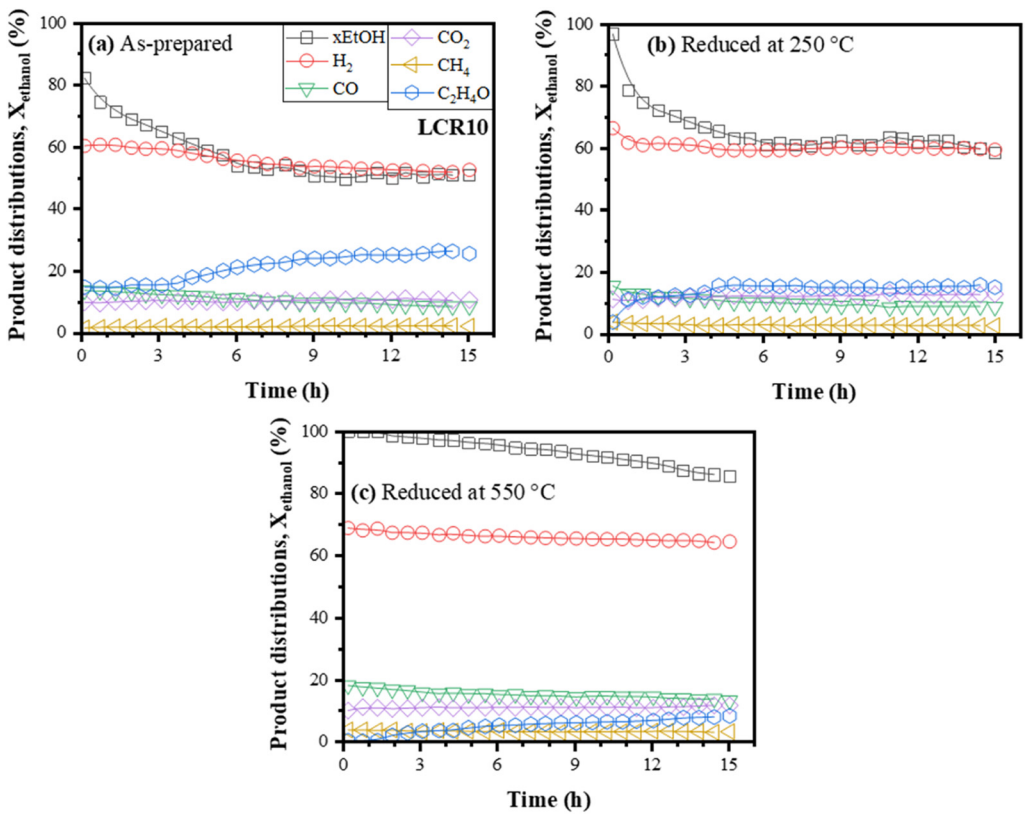

Fig. 3 Reduction temperature tests. Ethanol conversion (□, $X_{ethanol}$) and product distribution *versus* TOS for ESR over LCR10 at 600 °C without pre-reduction treatment (a), reduction at 250 °C before reaction (b), reduction at 550 °C before reaction, under H_2O/ethanol molar ratio = 3.0 (mass of catalyst = 10 mg and residence time = 0.010 g s mL^{-1}).

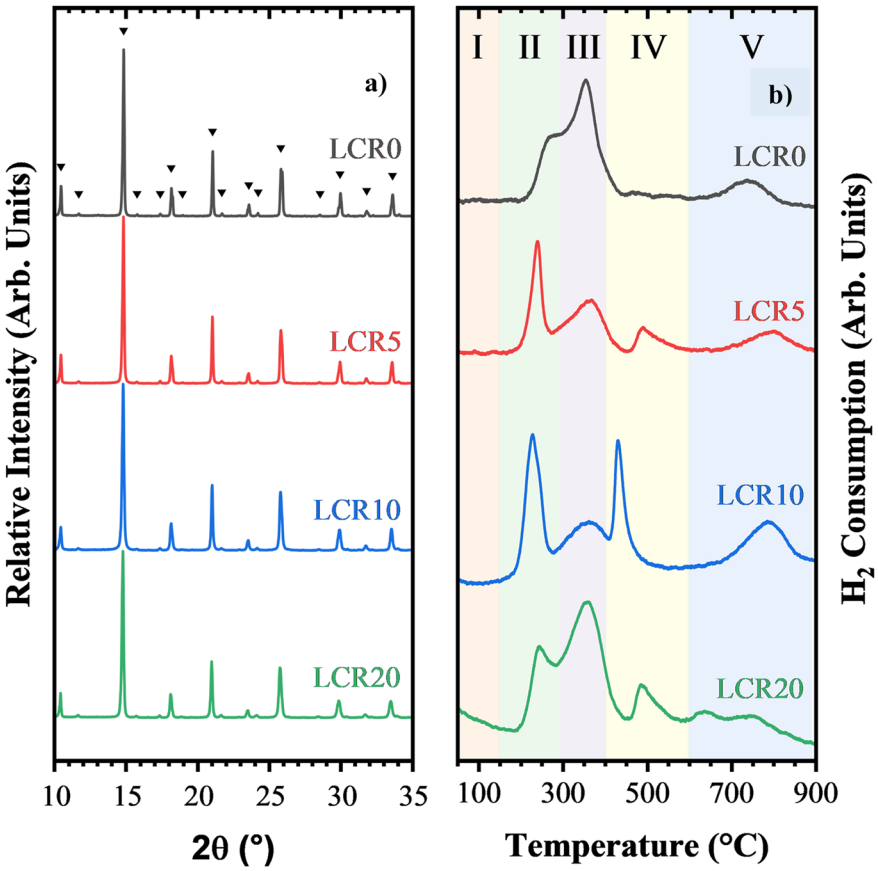

Fig. 4 Structural properties. (a) X-ray powder diffraction patterns for the $LaCr_{1-x}Ru_xO_3$ compounds. The peaks corresponding to the $LaCrO_3$ (▼) are indexed according to the *Pbmn* symmetry (ICSD #9938). (b) H_2-TPR profiles for the as-prepared samples.

atmosphere of the ESR reaction. It is important to note that such mild reduction conditions typically do not induce complete exsolution of 3D nanoparticles, which generally requires higher reduction temperatures.[5,20,27–29] Thus, these results indicate that LCR samples can be activated by the reducing environment of the ESR reaction, likely promoting the formation of highly active Ru species. This observation aligns with previous studies on ruthenium reduction under catalytic conditions, such as in dry reforming of methane.[21,46]

The catalytic tests for the LCR samples demonstrate that Ru-substituted $LaCrO_3$ exhibits outstanding catalytic properties for ESR. As widely accepted in ESR mechanisms, oxides promote the dehydrogenation of ethanol, while metallic species are required for C–C bond cleavage during reforming.[47–49] The catalysis data suggests that ESR catalytic active species are generated from ruthenium species in the solid solution in LCR oxide compounds. Moreover, the experimental data clearly differentiates the enhanced catalytic properties of the as-prepared LCR samples (Fig. 1) from that of both the impregnated reference and the samples reduced *ex situ* at 900 °C in H_2 (Fig. S2) The key finding is that the oxide single-phase LCR (Ru $x > 5\%$) catalysts are activated *in operando* under ESR conditions at 600 °C through a mild reduction promoted by the hydrogen generated during the reaction. Previous studies have shown the formation of active Ru exsolved nanoparticles in similar compounds. However, *ex situ* reduction for exsolution of nanoparticles usually requires significantly more severe reduction conditions than those of the ESR. As shown in Fig. 1 and 2, the active species derived from LCR solid solutions during ESR exhibit high resistance to deactivation and do not lead to carbon formation. Thus, further investigation is required to understand the effect of the Ru incorporated in the chromite lattice and the active species in the LCR samples.

3.4. Structural properties

Fig. 4a presents the X-ray powder diffraction (XRD) patterns of the LCR compounds. Additional XRD results for the impregnated and exsolved samples can be found in Fig. S5. All samples exhibit a single-phase structure, crystallizing in the *Pbnm* symmetry, consistent with the lanthanum chromite orthorhombic structure (ICSD#9938). No peaks corresponding to Ru compounds, such as Ru^0 or RuO_2, are observed, indicating that Ru is fully incorporated into the $LaCrO_3$ lattice. Within the detection limits of XRD, Ru-doped $LaCrO_3$ remains single-phase up to 20% at., confirming the formation of a solid solution.[20]

With increasing Ru doping, a shift in the XRD peaks is observed in Fig. 4a the substitution of Cr^{3+} (0.615 Å) with the slightly larger Ru^{3+} (0.68 Å) induces minor distortions in the orthorhombic structure.[50] The solid-solution formation is further evidenced by the dependence of the LCR lattice parameters on Ru content. Refined unit cell parameters increase linearly with Ru doping, following a Vegard-type relationship,[51] which strongly supports the formation of a solid solution (Fig. S5). Such an increase of the lattice volume is likely due to the slightly higher ionic radii of $Ru^{3+/4+}$ than that of Cr^{3+} and possible formation of oxygen defects upon Ru substitution. As shown in Fig. S5, samples reduced at high temperature (900 °C) display a small lattice volume decrease, which can be related to oxygen release and vacancy formation, as observed for the parent compound ($x = 0$). Such a decrease of the lattice volume is more pronounced at higher Ru content, indicating that ruthenium reduction also modifies the crystalline structure of the compound. Indeed, this is an indication of possible formation of Ru^0 that leaves the $LaCrO_3$ crystal lattice upon reduction.

The chemical composition and morphology of the LCR samples were examined using various techniques. Table 1 summarizes stoichiometric results obtained from Rietveld refinement (Table S1), wavelength-dispersive X-ray fluorescence (WDXRF), and energy-dispersive X-ray spectroscopy (EDS) (Table S2). WDXRF analysis confirmed that LCR samples have compositions close to the nominal values, consistent with EDS and Rietveld refinement data. While Ru contents in the LCR5 catalysts could not be measured due to X-ray wavelength limitations, both Rietveld refinement and EDS-derived La/Ru ratios align with nominal values. Furthermore, Rietveld refinement confirmed that Ru occupies the B-site of the perovskite lattice.

The temperature-programmed reduction (TPR) profile of the undoped LCR (Fig. 4b) exhibited two reduction peaks between 200 and 440 °C and a broad peak around 800 °C. The low-temperature peaks are associated with the reduction of surface Cr^{6+} (*T*-range II, ≈250 °C) and Cr^{4+} (*T*-range III, ≈350 °C), while the high-temperature peak (*T*-range V, ≈800 °C) corresponds to the reduction of bulk chromium species. Ru-doped samples displayed enhanced hydrogen consumption in regions II, III, and V (Table S3), along with the a new peak at ≈500 °C (*T*-range IV), which is attributed to Ru species in the $LaCrO_3$ lattice. These results suggest that Ru introduces new redox-active species and promotes the reducibility of Cr species contributing to H_2 consumption in distinct temperature regions, particularly at lower temperatures. The low-temperature peaks (*T*-range II and III) can be attributed to the reduction of surface Ru and Cr ions, while the high-temperature peaks (IV and V) correspond to bulk Ru and Cr species.[52]

Table 1 Chemical analysis. Ru/La stoichiometric molar ratios obtained from EDS analysis, site occupancy from Rietveld refinement, and WDXRF chemical composition of the samples

Sample	Nominal Ru/La (at%)	EDS	Rietveld	WDXRF
LCR0	—	—	—	—
LCR5	5	5(1)	6.2(3)	—
LCR10	10	9(1)	11.2(4)	12.1
LCR20	20	18(2)	17.5(4)	20.5

3.5. Microstructural analysis

Microstructural features of the samples were investigated using electron microscopy. Field-emission SEM (FEG-SEM) and aberration-corrected STEM (ACSTEM-EDS) analyses revealed significant details about the samples. The as-prepared powders, like the LCR10 shown in Fig. 4a, exhibit smooth and homogeneous surfaces characteristic of single-phase particles with an average size of ~100 nm. The relatively high calcination temperature (1000 °C) promoted well-defined rounded polygonal grains with discernable grain boundaries and no visible segregation or secondary phases, while retaining particles size in the nanometric domain. Such features are compatible with the refractory behavior of the $LaCrO_3$ perovskite. Upon further Ru doping, as in the LCR20 sample (Fig. S6) resulted in similar microstructure with no evidence of second phases, such as segregated RuO_2 at the surface that could be the source of metallic active ruthenium species. Such a segregation could be easily detected as shown by the SEM images of the reference impregnated sample (LCR-imp), which displayed elongated RuO_2 particles deposited on the surface of the perovskite, clearly observed by their brighter contrast compared to the $LaCrO_3$ matrix (Fig. S6).

A deeper assessment of the microstructure of the samples was performed by ACSTEM-EDS. Representative images from distinct regions of the as-prepared LCR10 sample showed a clean surface with homogeneous distribution of all elements, as shown in Fig. 5c and d. Therefore, high-resolution ACSTEM-EDS screening of the as-prepared sample LCR10 revealed single-phase oxide compound with no secondary phases.

To investigate possible formation of Ru species upon reduction, the LCR*x* samples were reduced *ex situ* at 900 °C under H_2 (samples referred to as LCR*x*-exs). FEG-SEM images of the LCR10-exs sample (Fig. 5b) indicate that the reduction treatment had no effect on the microstructure. Similarly to the LCR10, the exsolved samples exhibit clean surfaces and well-defined rounded particles with similar average size (~100 nm). However, higher magnification of the ACSTEM images (Fig. 5e and f) of the exsolved sample LCR10-exs revealed readily observable small protuberances on the surface. The ACSTEM image can be directly related to the corresponding EDS map in Fig. 5f in which the bright spots clearly exhibit a high concentration of Ru (in blue), which are further confirmed by TEM (Fig. S7). The rounded spots have estimated sizes spanning roughly from ~1 nm to 5 nm. Such a broad range of sizes suggests that different Ru species coexist on the sample reduced at 900 °C. The ACSTEM data indicate that these regions correspond to metallic Ru species,

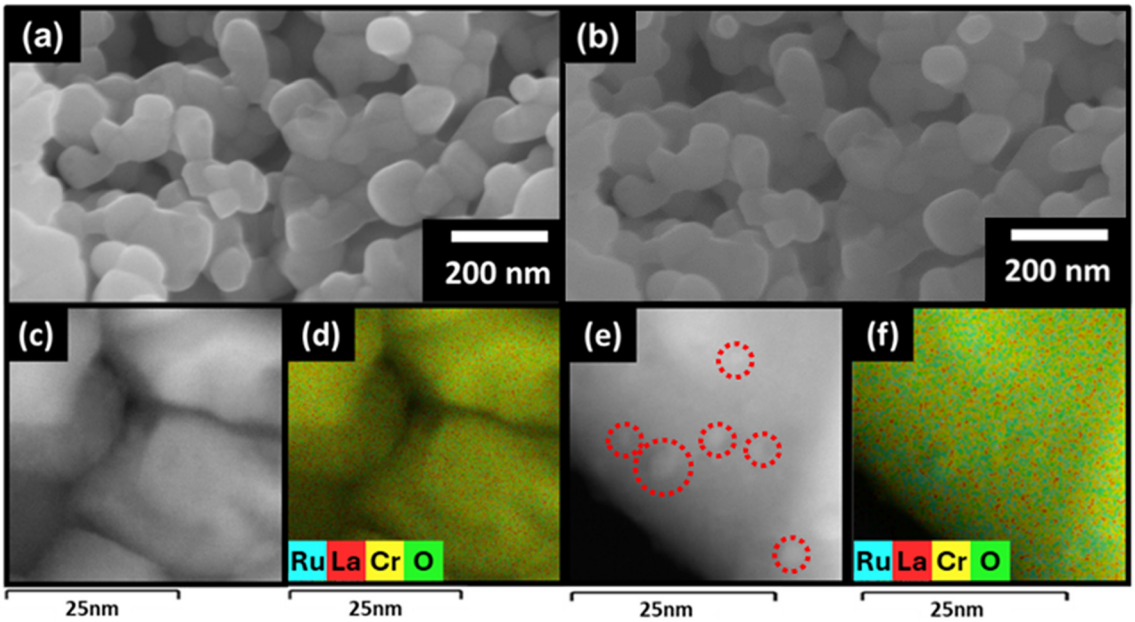

Fig. 5 Catalyst microstructure. FEG-SEM images of the as-prepared (a) LCR10 and (b) LCR10-exs. ACSTEM images and ACSTEM-EDS mapping of LCR10. (c) LCR10 ACSTEM image, (d) LCR10 combined Ru, La, Cr, and O EDS maps, (e) LCR10-exs ACSTEM image (f) LCR10-exs combined Ru, La, Cr, and O EDS maps, nanoparticles.

consistent with previous reports on Ru-doped $LaCrO_3$.[2,3] The electron microscopy analyses confirm that $La(Cr_{1-x}Ru_x)O_{3-\delta}$ (for $x \leq 0.20$) has no signs of segregated Ru or secondary Ru phases, *e.g.*, RuO_2, while upon reduction at high temperature (900 °C) metallic ruthenium species are formed. These findings strongly suggest that the outstanding catalytic properties of LCR ($x \geq 10$) are related to active metallic Ru species generated in the reducing conditions of ESR at 600 °C. Additional lower-magnification TEM images, provided in Fig. S8, further illustrate that the reduction and formation of these particles occur homogeneously throughout the sample rather than in isolated regions.

To confirm the formation of ruthenium species during ESR, the LCR20 sample was analyzed using high-resolution TEM (HR-TEM) under two conditions: as-prepared and post-ESR (600 °C). The HR-TEM analyses provide critical insights into the structural changes and active species formation during the reaction. The HR-TEM images of the as-prepared

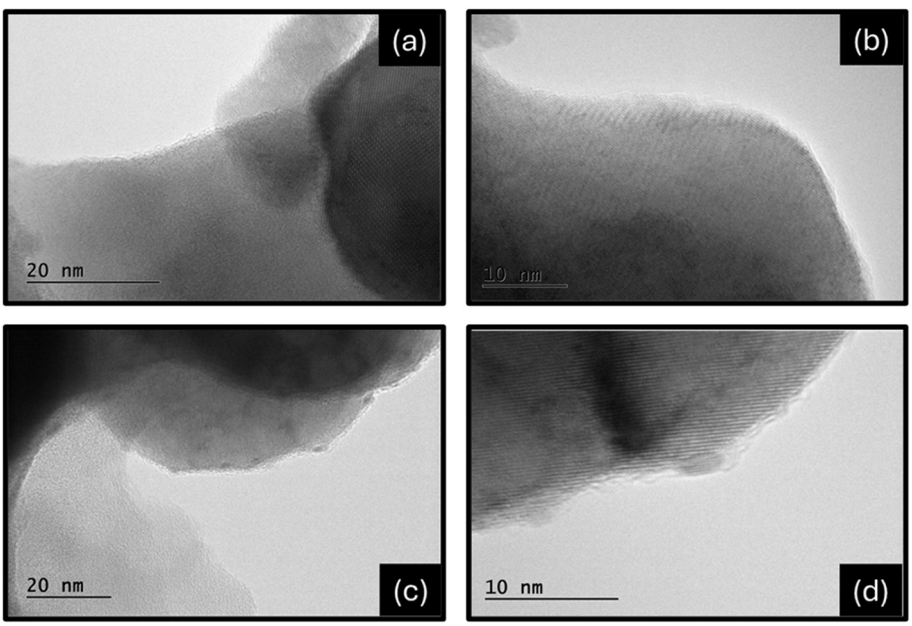

Fig. 6 Microstructure induced by ESR. HR-TEM images of the LCR20 compound: (a and b) as-prepared and (c and d) post ESR reaction at 600 °C.

LCR20 (Fig. 6a and b) reveal a single-phase crystalline structure devoid of noticeable segregations or nanoparticles. In contrast, post-ESR imaging (Fig. 6c and d) demonstrates the formation of small crystalline species. These highly dispersed Ru species formed during ESR (at 600 °C) have a size lower than 2 nm and are likely to be precursors to larger exsolved nanoparticles observed at higher reducing temperature (900 °C).

While Fig. 6c and d clearly illustrates the formation of sub-2 nm Ru species under ESR conditions at 600 °C, a direct comparison to exsolved nanoparticles formed after reduction at 900 °C (Fig. S7 and S8) reveals a broader distribution of particle sizes, often extending up to ~5 nm. The observed contrast between the small, highly dispersed Ru species post-ESR and the larger, more defined nanoparticles after high-temperature exsolution supports the *in operando* activation.

For LCR10, as discussed in Fig. 5 and S7, TEM and AC-STEM images confirmed the presence of exsolved Ru nanoparticles following the 900 °C reducing treatment, with sizes in a similar 1–5 nm range. However, due to challenges in locating a statistically significant number of Ru particles on the surface of the ESR-tested LCR10, particularly under low-temperature reduction (250–550 °C), a complete size distribution was not obtained. Nevertheless, the reduced number and smaller size of observable nanoparticles further support the *in operando* formation of dispersed Ru species under ESR conditions, consistent with the enhanced catalytic performance and the absence of carbon deposition.

This microstructural transformation highlights the generation of catalytically active Ru species at 600 °C under ESR conditions. Their size and dispersion suggest they play a critical role in the remarkable catalytic performance and activation mechanism of the LCR compounds. This supports the conclusion that the Ru species formed during ESR are key contributors to the superior catalytic behavior, offering insights into the fundamental properties governing the activation process.

3.6. Spectroscopic measurements

To investigate the Ru sites in the studied catalysts before and after reduction treatments, detailed XPS and XAS analyses

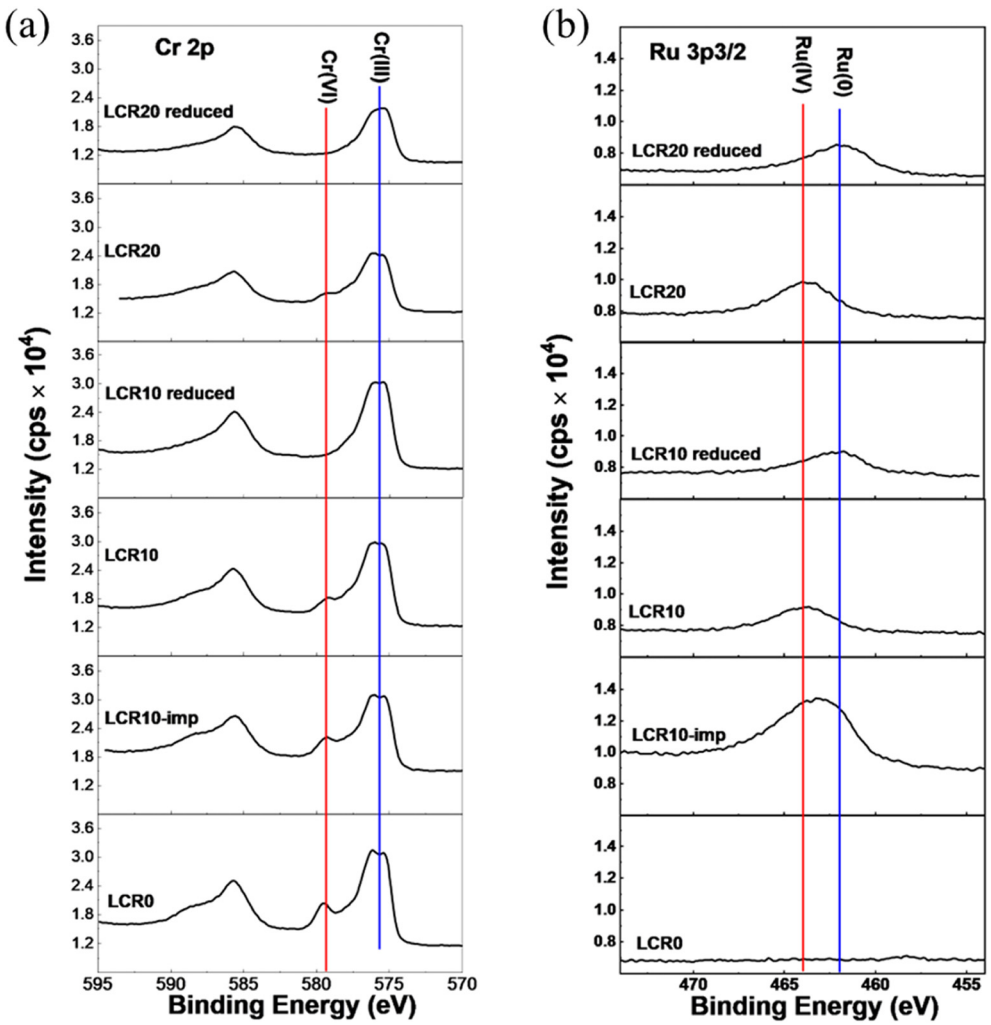

Fig. 7 XPS analysis of the Ru-doped lanthanum chromite and impregnated powders XPS spectra for (a) Cr 2p and (b) Ru $3p_{3/2}$ energy regions.

were performed. Fig. 7 presents the XPS results for both as-prepared and reduced (at 900 °C) samples. The XPS spectra for lanthanum (La3d3/2 and La3d5/2) showed no significant dependence on Ru doping or the reduction treatment (Fig. S9), supporting the substitution of Ru at the B-site of the perovskite structure. In contrast, the chromium and ruthenium species exhibited notable changes upon Ru doping and reduction treatment.

For Cr 2p, in addition to the expected bulk Cr^{3+}, a peak corresponding to Cr^{6+} was detected (Fig. 7a). Previous studies have associated Cr^{6+} with surface-segregated $LaCrO_4$, a tetragonal phase observed in samples calcined at low temperatures (~600 °C).[20,21,53] However, no crystalline secondary phases were identified, suggesting that defective surfaces of $LaCrO_3$ can stabilize chromium species with higher oxidation states than the bulk Cr^{3+}. The Cr^{6+} peak was more pronounced in LCR0 than in Ru-doped samples, suggesting that Ru substitution suppresses the oxidation of Cr^{3+} to Cr^{6+}. This effect is likely due to charge transfer between Ru and oxygen at the $LaCrO_3$ surface, indicating strong Ru-chromite interactions.[21]

The XPS data also revealed that Ru in LCR samples exhibits a $Ru^{4+\Delta}$ ionic state (Fig. 7b). The binding energy of Ru incorporated into the perovskite structure was higher than that of Ru^{4+} in RuO_2 (463 eV),[54,55] pointing to a mixed-valence state of Ru within the lattice rather than on the surface. Similarly to Cr^{6+}, Ru^{4+} may be linked to defective or distorted surface structures. Previous studies on Ru-doped $LaCrO_3$ have distinguished between lattice Ru and surface/lattice-segregated Ru clusters resembling RuO_2.[56] However, such segregation was only observed at doping levels exceeding the solubility limit ($x > 0.20$),[20] whereas in the present study no evidence of segregation was found.

The reference impregnated sample (LCR10-imp) exhibited a mixture of Ru^{4+} and Ru^0 species after calcination at 700 °C in air. The Ru in this sample forms isolated, partially reduced Ru^0 particles, which become coated with an oxidized RuO_2 (Ru^{4+}) layer upon exposure to air. These results highlight the distinction between Ru species in the impregnated catalyst and those incorporated into the lattice of LCR ceramic powders.

To gain further insights into the LCR samples, synchrotron experiments were conducted, focusing on Ru K-edge XANES spectra for both as-prepared and *in situ* reduced at 550 °C samples (Fig. S10). The *in situ* XAS reduction temperature was chosen to mimic conditions close to those experienced during the ESR reaction at 600 °C (Fig. 1). Details of the XAS experiments are provided in Table S4. For catalysts previously reduced at 900 °C air oxidation leads to full oxidation of the metallic Ru NPs, for example, the bottom spectrum in Fig. 8b. *In situ* XAS reduction at 550 °C is high enough to reduce air oxidized surface Ru to metallic NPs without further changes in the particle size or amount of surface Ru.

The XANES spectra for as-prepared LCR5, LCR10, and LCR20 samples (Fig. 8) were identical, indicating that Ru is

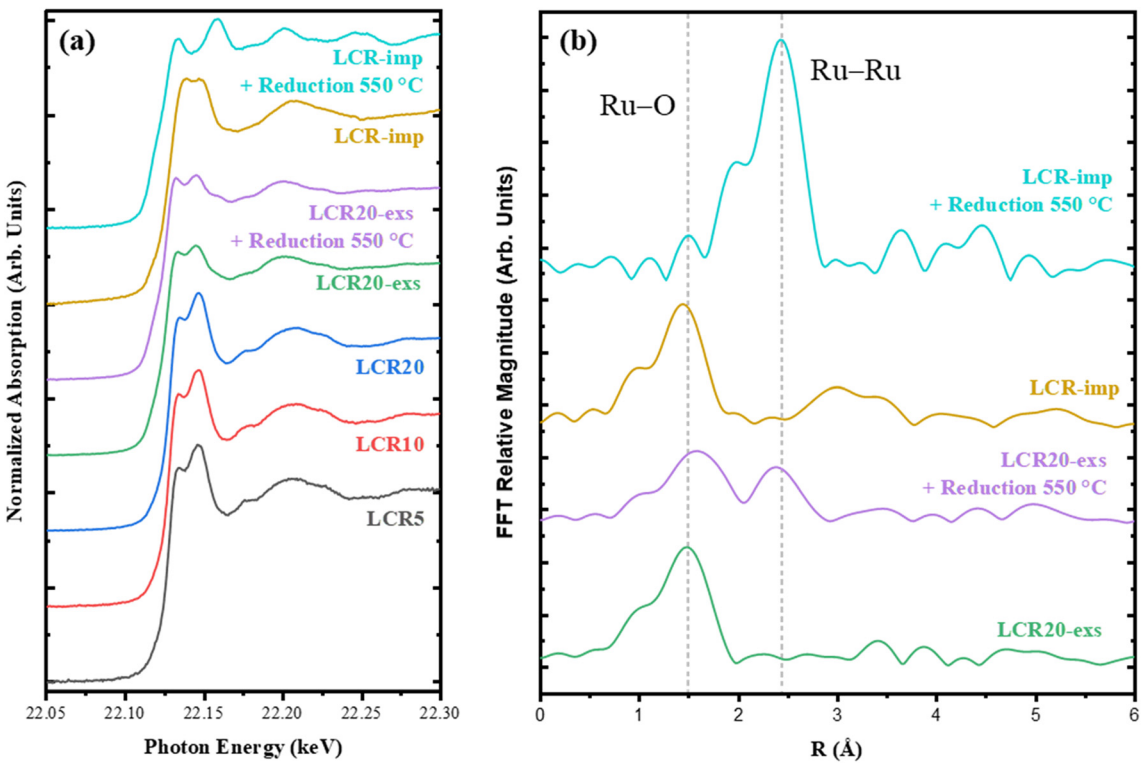

Fig. 8 Chemical evolution upon reduction. Ru K-edge XANES spectra from 22.05–22.3 keV (a) and Fourier transformed Ru K-edge EXAFS spectra (b).

present predominantly as Ru^{4+}, with six Ru–O bonds at 2.01 Å (Table S4). This bond length is slightly larger than the expected for RuO_2 (1.98 Å), likely reflecting a distorted $Ru^{\Delta+}O_{6-\delta}$ octahedral configuration in the perovskite structure. These findings corroborate the absence of segregated RuO_2, a phenomenon typically observed in LCR samples with Ru concentrations exceeding 0.20 at% ($x > 0.20$).[20]

Upon *in situ* reduction at 550 °C, the XANES spectra for LCR10 and LCR20 revealed the formation of a small fraction of metallic Ru, being 5% and 10%, respectively. Such values were estimated through linear combination fitting of the calcined LCR spectra with a reference Ru nanoparticle (NP) spectrum (Fig. S11). The observed changes in the XANES spectra, including shifts to lower energy and alterations in peak shape, are consistent with partial reduction of Ru. Fitting the first-shell Ru–O coordination peak (≈1.5 Å, phase uncorrected distance) indicated a slight decrease in the number of Ru–O bonds from 6.0 in the calcined samples to 5.7 in the reduced samples (Table S4), suggesting a partial reduction of oxidized Ru. Unfortunately, the fraction of metallic Ru NPs, appearing at distances of 1.7–2.9 Å, was too faint to allow reliable quantitative fitting.

The XANES data confirm that catalytically active ruthenium species are generated under reducing conditions similar to that used for ESR. These active species likely originate from ionic Ru^{4+} within a distorted perovskite surface termination structure ($BO_{6-\delta}$), such as partially reduced $(Cr, Ru)^{\Delta+}O_{6-\delta}$, which accommodates higher valence Ru ions. Interestingly, EXAFS data fitting for LCR samples revealed that Ru coordination deviates from that of fully oxidized RuO_2 (Fig. 8b), supporting the idea that active Ru species reside on the defective, surface-exposed crystalline planes of the perovskite structure. These sites are highly sensitive to reducing conditions, contributing to the outstanding catalytic properties observed in LCR samples with doping ratios above 10%.

Additionally, XAS data highlight the distinct ruthenium species present in the samples. For the LCR-imp sample, the as-prepared state exhibited 100% Ru^{4+} with six Ru–O bonds at 1.97 Å. The XANES fitting revealed that the Ru–O bond length in LCR-imp is shorter than that in the LCR samples but comparable to RuO_2. Such different bond lengths indicate a different coordination environment (CN) for the impregnated Ru compared to the Ru in the solid-solution. This distinction strongly suggests that the Ru in LCR is structurally integrated into the perovskite, whereas the impregnated Ru likely forms segregated RuO_2-like species. Such features may account for the enhanced catalytic properties of the as-prepared LCR*x* samples.

Upon reduction at 550 °C, the LCR-imp sample displayed complete reduction of Ru^{4+} to Ru^0 (Fig. 8b). EXAFS analysis confirmed a Ru–Ru CN of 10.9 at 2.67 Å, closely resembling the values for the metallic Ru foil reference (CN = 12 at 2.68 Å). These values correspond to nanoparticles with an estimated diameter of ~7 nm. Similarly, the Ru impregnated on SiO_2 exhibited an XANES spectrum consistent with LCR-imp, with a Ru–Ru CN of 11.4 at 2.68 Å, corresponding to nanoparticle sizes of 8–9 nm. Importantly, the reduced Ru particles in both reference samples remained stable and did not oxidize when exposed to air at room temperature.

The combination of XPS, XAS, TPR, and electron microscopy provides a comprehensive view of the Ru-doped $LaCrO_3$ compounds. XPS revealed high oxidation states for Ru and Cr on the surface, while XAS confirmed Ru^{4+} integration within the perovskite structure, with a longer Ru–O bond than in RuO_2. TPR and XAS demonstrated that surface Ru species are readily reduced to Ru^0 under ESR conditions. These findings align with prior studies on $LaCr_{0.95}Ru_{0.05}O_3$, which was shown to be an effective catalyst for heavy hydrocarbon fuels.[16,21] In that compound, Ru was atomically dispersed at the B-site, with a concentration at the surface as ionic species, where oxygen coordination was incomplete at crystallite interfaces.[16] Similarly, the present study shows that surface Ru ionic species in LCR react with hydrogen during TPR (or ethanol during ESR), forming catalytically active Ru^0 particles.

3.7. Thermo-chemical mechanism

Based on our findings, Fig. 9 schematically illustrates the interplay between surface characteristics, oxidation, reduction, and the resulting particle configurations. Exposed $(Cr, Ru)^{\Delta+}O_{6-\delta}$ octahedral terminations likely serve as the source of surface-distributed Ru ionic species, which reduce to finely dispersed Ru^0 particles. These active metallic particles, comprising limited numbers of Ru atoms, resemble single-atom configurations derived from ionic species in solid solution (Fig. 9b). Similar transformations of surface Ru species into small metallic ensembles have been observed in other materials[17,18,57] and more in $LaCr_{1-x}Ru_xO_3$.[21,58] While these metallic Ru species are difficult to detect *via* electron microscopy (as in Fig. 5), their exceptional catalytic properties align well with previous reports.[16–18,21,56,57]

The combined experimental results demonstrate that the catalytic activity of LCR is closely tied to both the ruthenium valence state ($Ru^{\Delta+}/Ru^0$) and the origin of the active Ru species. In the LCR10 catalyst, XAS measurements revealed the presence of Ru^0 after reduction at 550 °C, correlating with the H_2 consumption observed at 205 °C in the TPR. This indicates that ESR reaction conditions at 600 °C facilitate the reduction of $Ru^{\Delta+}$ species on the catalyst surface, leading to the formation of catalytically active sites, as observed in post-ESR HRTEM images. These reduced or partially reduced Ru species are critical for the stable conversion of ethanol, as evidenced by the performance of the LCR10 sample.

These active species likely form as small particles or clusters derived from partially reduced Ru sites, as suggested by HR-TEM observations (Fig. 6 and S7). Importantly, they do not originate from segregated RuO_2, but from surface-localized ruthenium species in the $LaCr_{1-x}Ru_xO_3$. The propensity of these $Ru^{\Delta+}$ ensembles to undergo reduction, as

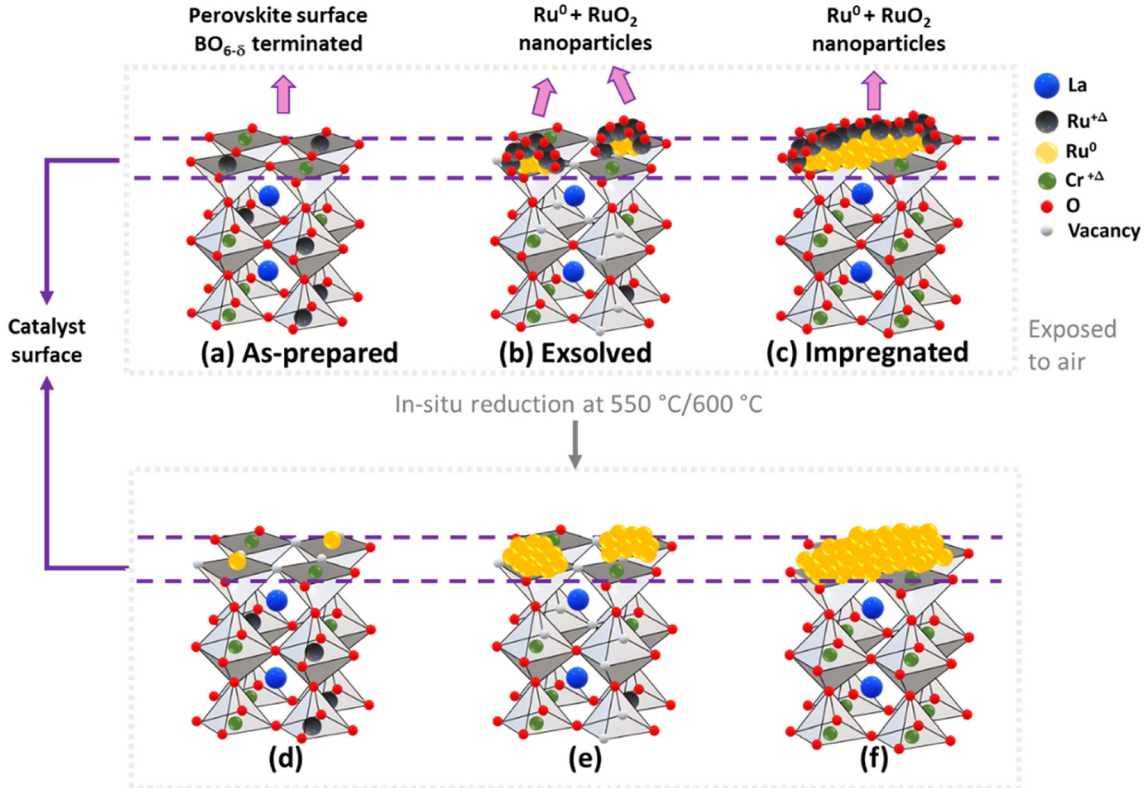

Fig. 9 Ru from ionic species to active catalyst. Schematic representation of the Ru species in Ru-doped lanthanum chromite perovskite surfaces: (a and d) as-prepared, (b and e) exsolved at 900 °C, and (c and f) impregnated samples. Upper panel: in air. Down panel: surface Ru species after *in situ* reduction at 550 °C (Ru and RuO_2 clusters/particles are not in scale).

confirmed by TPR and XAS measurements, underscores their catalytic relevance. Reduction of $LaCr_{1-x}Ru_xO_3$ at higher temperature (900 °C) leads to exsolution of larger Ru^0 nanoparticles, whilst the small Ru species formed *in operando* during ESR reaction exhibit distinctive catalytic properties. The metallic active sites achieved by the exsolution under mild (ESR) conditions confer strong interaction between the nanometric active particles and the oxide matrix. Such enhanced physico-chemical interaction of the solid-solution derived active sites is comparatively stronger than that in impregnated samples and promotes anti-coking properties. Soaked Ru metallic active sites are pinned at the perovskite surface impeding filamentary carbon base growth, while oxygen vacancies formed upon reduction of the perovskite oxidize amorphous carbon deposit contributing to inhibit coking during ESR.

4. Conclusions

The study of Ru-substituted lanthanum chromite ($LaCr_{1-x}Ru_xO_{3-\delta}$) solid solutions for ethanol steam reforming (ESR) reveals that while the $LaCrO_3$ parent compound is inactive for the reaction, the Ru-substituted perovskites are single-phase and highly active for hydrogen production. The best catalytic properties are achieved for oxide samples activated *in operando* during the ESR at 600 °C and are attributed to small metallic ruthenium species.

Detailed characterization showed that catalytic active Ru species originate from Ru ionic species in the $LaCr_{1-x}Ru_xO_{3-\delta}$ compounds. The EXAFS data reveal that the bond length of Ru in these samples differs from that in segregated RuO_2, suggesting that defective $Ru^{\Delta+}O_{6-\delta}$ octahedra on the surface of the perovskite structure are the preferable source of easily reducible ruthenium species. These $Ru^{4+\Delta}$ ions are the precursor to highly active metallic ruthenium species for ethanol steam reforming. This mechanism aligns with the generation of exsolved Ru nanoparticles observed at higher reducing temperatures, indicating that active Ru species emerge from the mixed-oxide matrix in different ways depending on the reduction treatment. Reduction at 900 °C results in larger exsolved nanoparticles that coexist with the small Ru species obtained at ESR conditions. Catalytic tests revealed that the outstanding stability and coke resistance after 200 hours of ESR are ascribed to the small species obtained at mild reduction conditions of the ESR reaction, which have a strong interaction with the oxide matrix.

Synchrotron X-ray absorption data under mild reduction conditions (similar to those in ESR) confirmed that Ru^{4+} species are reduced to highly active Ru^0 species, which are similar to previously reported single-atom catalysts. Such

particles could be observed in HRTEM analysis of the samples $LaCr_{1-x}Ru_xO_3$ post ESR reaction.

The experimental results show that controlling the reduction of solid-solution dispersed ionic Ru species in refractory mixed-valence oxide surfaces is an effective strategy for generating highly active catalytic particles for reactions like ethanol steam reforming.

Author contributions

Tamara S. Moraes: methodology, validation, investigation, data curation, writing – original draft, writing – review & editing, visualization. Victor B. Tinti: methodology, validation, investigation, data curation, formal analysis, investigation, writing – original draft, writing – review & editing, visualization. Fernando Piazzolla: investigation. Daniel Z. de Florio: resources, supervision. Andre S. Ferlauto: writing – review & editing, supervision. Yohei Miura: formal analysis, investigation. David P. Dean: formal analysis, investigation. Jeffrey T. Miller: formal analysis, investigation, writing – review & editing. Abhaya K. Datye: formal analysis, writing – review & editing. Hien N. Pham: formal analysis, investigation. Fabio C. Fonseca: conceptualization, resources, writing – review & editing, supervision, project administration, funding acquisition.

Conflicts of interest

There are no conflicts to declare.

Data availability

Supplementary characterization of samples (TG/DTA, XRD, FEG-SEM, ACSTEM, TEM, XAS). Structural and microstructural characterization of samples reduced at 900 °C. Ethanol steam reforming properties and spent catalysts analyses. See DOI: **https://doi.org/10.1039/D5CY00774G**.

Data for this article, including XRD, catalysis testing, XPS, SAX, and TPR are available at IPEN repository at **https://repositorio.ipen.br/**.

Acknowledgements

The authors are thankful for the support of Brazilian agencies CNPq (Sis-H2 407967/2022-2) and FAPESP (17/11937-4, 19/15110-2, 19/00776-5, 21/12459-4, and 23/14931-8). FCF and ASF are CNPq fellows. FCF is thankful for Nissan's partial funding. R. Abe, R. M Guimarães (Nissan Brazil) and Y. Fukuyama (Nissan Japan) are acknowledged for fruitful discussions and kind support. Acquisition of the AC-STEM at UNM was supported by NSF DMR-1828731. Use of the Center for Nanoscale Materials and Advanced Photon Source, both Office of Science user facilities, was supported by the U.S. Department of Energy, Office of Science, Office of Basic Energy Sciences, under Contract No. DE-AC02-06CH11357. MRCAT operations and the beamline 10-BM were supported by the Department of Energy and the MRCAT member institutions. D. P. D., J. T. M., H. N. P. and A. K. D. also acknowledge support from the NSF/ERC CISTAR which is supported by the National Science Foundation under Cooperative Agreement No. EEC-1647722 and by the C2C supplemental funding. Authors are thankful for the support given by the Radiation Technology Center (IPEN) for the Raman experiments (Finep, grant: 01.18.0073.00) and the CNPEM projects 20220620 (XPS), 20230423 (TEM).

References

1 C. C. Geddes, I. U. Nieves and L. O. Ingram, Advances in ethanol production, *Curr. Opin. Biotechnol.*, 2011, **22**, 312–319, DOI: **10.1016/j.copbio.2011.04.012**.

2 R. Muccillo, E. N. S. Muccillo, F. C. Fonseca and D. Z. de Florio, Characteristics and Performance of Electrolyte-Supported Solid Oxide Fuel Cells under Ethanol and Hydrogen, *J. Electrochem. Soc.*, 2008, **155**, B232, DOI: **10.1149/1.2828024**.

3 A. A. A. da Silva, M. C. Steil, F. N. Tabuti, R. C. Rabelo-Neto, F. B. Noronha, L. V. Mattos and F. C. Fonseca, The role of the ceria dopant on Ni/doped-ceria anodic layer cermets for direct ethanol solid oxide fuel cell, *Int. J. Hydrogen Energy*, 2021, **46**, 4309–4328, DOI: **10.1016/j.ijhydene.2020.10.155**.

4 A. Haryanto, S. Fernando, N. Murali and S. Adhikari, Current Status of Hydrogen Production Techniques by Steam Reforming of Ethanol: A Review, *Energy Fuels*, 2005, **19**, 2098–2106, DOI: **10.1021/ef0500538**.

5 L. Guerrero, S. Castilla and M. Cobo, Advances in Ethanol Reforming for the Production of Hydrogen, *Quim. Nova*, 2014, **37**(5), 850–856, DOI: **10.5935/0100-4042.20140137**.

6 A. Boretti, Advantages of converting Diesel engines to run as dual fuel ethanol–Diesel, *Appl. Therm. Eng.*, 2012, **47**, 1–9, DOI: **10.1016/j.applthermaleng.2012.04.037**.

7 M. Balat and H. Balat, Recent trends in global production and utilization of bio-ethanol fuel, *Appl. Energy*, 2009, **86**, 2273–2282, DOI: **10.1016/j.apenergy.2009.03.015**.

8 J. Vicente, C. Montero, J. Ereña, M. J. Azkoiti, J. Bilbao and A. G. Gayubo, Coke deactivation of Ni and Co catalysts in ethanol steam reforming at mild temperatures in a fluidized bed reactor, *Int. J. Hydrogen Energy*, 2014, **39**, 12586–12596, DOI: **10.1016/j.ijhydene.2014.06.093**.

9 P. Vernoux, Lanthanum chromite as an anode material for solid oxide fuel cells, *Ionics*, 1997, **3**, 270–276, DOI: **10.1007/BF02375628**.

10 J. Fergus, Lanthanum chromite-based materials for solid oxide fuel cell interconnects, *Solid State Ionics*, 2004, **171**, 1–15, DOI: **10.1016/j.ssi.2004.04.010**.

11 S. Gupta, M. K. Mahapatra and P. Singh, Phase transformation, thermal expansion and electrical conductivity of lanthanum chromite, *Mater. Res. Bull.*, 2013, **48**, 3262–3267, DOI: **10.1016/j.materresbull.2013.05.032**.

12 N. Sakai, T. Kawada, H. Yokokawa, M. Dokiya and T. Iwata, Sinterability and electrical conductivity of calcium-doped lanthanum chromites, *J. Mater. Sci.*, 1990, **25**, 4531–4534, DOI: **10.1007/BF00581119**.

13 A. Umar and M. O. Thotyl, Perovskite modified catalysts with improved coke resistance for steam reforming of glycerol to renewable hydrogen fuel, *GCB Bioenergy*, 2023, **15**, 791–804, DOI: **10.1111/gcbb.13050**.

14 D. Neagu, T.-S. Oh, D. N. Miller, H. Ménard, S. M. Bukhari, S. R. Gamble, R. J. Gorte, J. M. Vohs and J. T. S. Irvine, Nano-socketed nickel particles with enhanced coking resistance grown in situ by redox exsolution, *Nat. Commun.*, 2015, **6**, 8120, DOI: **10.1038/ncomms9120**.

15 J. Bak, H. B. Bae and S.-Y. Chung, Atomic-scale perturbation of oxygen octahedra via surface ion exchange in perovskite nickelates boosts water oxidation, *Nat. Commun.*, 2019, **10**, 2713, DOI: **10.1038/s41467-019-10838-1**.

16 D. Liu and M. Krumpelt, Activity and Structure of Perovskites as Diesel-Reforming Catalysts for Solid Oxide Fuel Cell, *Int. J. Appl. Ceram. Technol.*, 2005, **2**, 301–307, DOI: **10.1111/j.1744-7402.2005.02032.x**.

17 A. C. W. Koh, L. Chen, W. K. Leong, T. P. Ang, B. F. G. Johnson, T. Khimyak and J. Lin, Ethanol steam reforming over supported ruthenium and ruthenium–platinum catalysts: Comparison of organometallic clusters and inorganic salts as catalyst precursors, *Int. J. Hydrogen Energy*, 2009, **34**, 5691–5703, DOI: **10.1016/j.ijhydene.2009.05.044**.

18 A. C. W. Koh, W. K. Leong, L. Chen, T. P. Ang, J. Lin, B. F. G. Johnson and T. Khimyak, Highly efficient ruthenium and ruthenium–platinum cluster-derived nanocatalysts for hydrogen production via ethanol steam reforming, *Catal. Commun.*, 2008, **9**, 170–175, DOI: **10.1016/j.catcom.2007.05.034**.

19 N. K. Monteiro, F. B. Noronha, L. O. O. da Costa, M. Linardi and F. C. Fonseca, A direct ethanol anode for solid oxide fuel cell based on a chromite-manganite with catalytic ruthenium nanoparticles, *Int. J. Hydrogen Energy*, 2012, **37**, 9816–9829, DOI: **10.1016/j.ijhydene.2012.03.157**.

20 Y. Jeon, O. Kwon, C. Lee, G. Lee, J. Myung, S. Sun Park, J. T. S. Irvine and Y. Shul, Positional influence of Ru on Perovskite structured catalysts for efficient H2 production process by heavy-hydrocarbon source, *Appl. Catal., A*, 2019, **582**, 117111, DOI: **10.1016/j.apcata.2019.117111**.

21 H. Yu, Y. Wang, X. Tao, F. Yu, T. Zhao, M. Li and H. Wang, Interfacial Metal–Support Interaction and Catalytic Performance of Perovskite LaCrO3-Supported Ru Catalyst, *ACS Appl. Mater. Interfaces*, 2024, **16**, 17483–17492, DOI: **10.1021/acsami.3c19119**.

22 T. Wan, F. Jin, X. Cheng, J. Gong, C. Wang, G. Wu and A. Liu, Influence of hydrophilicity and titanium species on activity and stability of Cr/MWW zeolite catalysts for dehydrogenation of ethane with CO2, *Appl. Catal., A*, 2022, **637**, 118542, DOI: **10.1016/j.apcata.2022.118542**.

23 H. S. Bengaard, J. K. Nørskov, J. Sehested, B. S. Clausen, L. P. Nielsen, A. M. Molenbroek and J. R. Rostrup-Nielsen, Steam Reforming and Graphite Formation on Ni Catalysts, *J. Catal.*, 2002, **209**, 365–384, DOI: **10.1006/jcat.2002.3579**.

24 Q. Guo, J. Geng, J. Pan, B. Chi, C. Xiong and J. Pu, A-site deficient La1-xCr0.95Ru0.05O3-δ perovskites for N-hexadecane steam reforming: Effect of steam activation and active oxygen, *Renewable Energy*, 2023, **219**, 119495, DOI: **10.1016/j.renene.2023.119495**.

25 P. Vernoux, J. Guindet and M. Kleitz, Gradual Internal Methane Reforming in Intermediate-Temperature Solid-Oxide Fuel Cells, *J. Electrochem. Soc.*, 1998, **145**(10), 3487, DOI: **10.1149/1.1838832**.

26 S. G. M. Carvalho, F. N. Tabuti, E. I. Santiago, R. Abe, R. M. Guimaraes, Y. Miura, Y. Fukuyama and F. C. Fonseca, Advancing direct ethanol metal supported fuel cells with catalytic layer, *Mater. Sci. Eng., B*, 2025, **318**, 118259, DOI: **10.1016/j.mseb.2025.118259**.

27 K. Kousi, C. Tang, I. S. Metcalfe and D. Neagu, Emergence and Future of Exsolved Materials, *Small*, 2021, **17**, 2006479, DOI: **10.1002/smll.202006479**.

28 V. B. Tinti, D. Marani, A. S. Ferlauto, F. C. Fonseca, V. Esposito and D. Z. Florio, Exsolution of Nickel Nanoparticles from Mixed-Valence Metal Oxides: A Quantitative Evaluation by Magnetic Measurements, *Part. Part. Syst. Charact.*, 2020, **37**, 1900472, DOI: **10.1002/ppsc.201900472**.

29 T.-S. Oh, E. K. Rahani, D. Neagu, J. T. S. Irvine, V. B. Shenoy, R. J. Gorte and J. M. Vohs, Evidence and Model for Strain-Driven Release of Metal Nanocatalysts from Perovskites during Exsolution, *J. Phys. Chem. Lett.*, 2015, **6**, 5106–5110, DOI: **10.1021/acs.jpclett.5b02292**.

30 D. Neagu, G. Tsekouras, D. N. Miller, H. Ménard and J. T. S. Irvine, In situ growth of nanoparticles through control of non-stoichiometry, *Nat. Chem.*, 2013, **5**, 916–923, DOI: **10.1038/nchem.1773**.

31 Y. H. Kim, H. Jeong, B.-R. Won, H. Jeon, C. Park, D. Park, Y. Kim, S. Lee and J. Myung, Nanoparticle Exsolution on Perovskite Oxides: Insights into Mechanism, Characteristics and Novel Strategies, *Nano-Micro Lett.*, 2024, **16**, 33, DOI: **10.1007/s40820-023-01258-4**.

32 S. Lou, X. Meng, N. Liu and L. Shi, A-site defects boosted exsolution on (La0.5Ca0.5)(1-α)Ni0.06Ti0.94O3-δ for ethanol steam reforming, *Chem. Eng. J.*, 2023, **476**, 146145, DOI: **10.1016/j.cej.2023.146145**.

33 S. Lou, X. Meng, N. Liu and L. Shi, A-site deficient titanate perovskite surface with exsolved nickel nanoparticles for ethanol steam reforming, *Chem. Eng. Sci.*, 2023, **274**, 118690, DOI: **10.1016/j.ces.2023.118690**.

34 X.-F. Yang, A. Wang, B. Qiao, J. Li, J. Liu and T. Zhang, Single-Atom Catalysts: A New Frontier in Heterogeneous Catalysis, *Acc. Chem. Res.*, 2013, **46**, 1740–1748, DOI: **10.1021/ar300361m**.

35 C. Riley, A. De La Riva, S. Zhou, Q. Wan, E. Peterson, K. Artyushkova, M. D. Farahani, H. B. Friedrich, L. Burkemper, N. Atudorei, S. Lin, H. Guo and A. Datye, Synthesis of Nickel-Doped Ceria Catalysts for Selective Acetylene Hydrogenation, *ChemCatChem*, 2019, **11**, 1526–1533, DOI: **10.1002/cctc.201801976**.

36 M. P. Pechini, Method of Preparing Lead and Alkaline Earth Titanates and Niobates and Coating Method Using the Same to Form a Capacitor, *US Pat.*, 3330697, 1967.

37 D. Segal, Chemical synthesis of ceramic materials, *J. Mater. Chem.*, 1997, **7**, 1297–1305, DOI: **10.1039/a700881c**.

38 H. M. Rietveld, A profile refinement method for nuclear and magnetic structures, *J. Appl. Crystallogr.*, 1969, **2**, 65–71, DOI: **10.1107/S0021889869006558**.

39 A. A. Coelho, TOPAS and TOPAS-Academic : an optimization program integrating computer algebra and crystallographic objects written in C++, *J. Appl. Crystallogr.*, 2018, **51**, 210–218, DOI: **10.1107/S1600576718000183**.

40 T. S. Moraes, R. C. R. Neto, M. C. Ribeiro, L. V. Mattos, M. Kourtelesis, S. Ladas, X. Verykios and F. B. Noronha, Ethanol conversion at low temperature over CeO2—Supported Ni-based catalysts. Effect of Pt addition to Ni catalyst, *Appl. Catal., A*, 2016, **181**, 754–768, DOI: **10.1016/j.apcatb.2015.08.044**.

41 Z. Li, L. Deng, I. A. Kinloch and R. J. Young, Raman spectroscopy of carbon materials and their composites: Graphene, nanotubes and fibres, *Prog. Mater. Sci.*, 2023, **135**, 101089, DOI: **10.1016/j.pmatsci.2023.101089**.

42 A. C. Ferrari, J. C. Meyer, V. Scardaci, C. Casiraghi, M. Lazzeri, F. Mauri, S. Piscanec, D. Jiang, K. S. Novoselov, S. Roth and A. K. Geim, Raman Spectrum of Graphene and Graphene Layers, *Phys. Rev. Lett.*, 2006, **97**, 187401, DOI: **10.1103/PhysRevLett.97.187401**.

43 M. N. Iliev, A. P. Litvinchuk, V. G. Hadjiev, Y.-Q. Wang, J. Cmaidalka, R.-L. Meng, Y.-Y. Sun, N. Kolev and M. V. Abrashev, Raman spectroscopy of low-temperature (Pnma) and high-temperature (R3c) phases of LaCrO3, *Phys. Rev. B: Condens. Matter Mater. Phys.*, 2006, **74**, 214301, DOI: **10.1103/PhysRevB.74.214301**.

44 J. Guo, J. Zhang, G. Wang, W. Geng, C. Zheng and Y. Chai, Characteristic and Kinetics of Oxidation of Coke by CO2 Based on Isothermal Method, in *6th Int. Symp. High-Temperature Metall. Process.*, Springer International Publishing, Cham, 2015, pp. 619–626, DOI: **10.1007/978-3-319-48217-0_79**.

45 M. Wang, G. Wei, R. Zhu and K. Dong, Effect of CO2-O2 oxidizing atmospheres on the combustion characteristics of metallurgical coke and anthracite, *J. CO2 Util.*, 2021, **52**, 101665, DOI: **10.1016/j.jcou.2021.101665**.

46 A.-L. Sauvet and J. Fouletier, Electrochemical properties of a new type of anode material La1−xSrxCr1−yRuyO3−δ for SOFC under hydrogen and methane at intermediate temperatures, *Electrochim. Acta*, 2001, **47**, 987–995, DOI: **10.1016/S0013-4686(01)00811-8**.

47 P. D. Vaidya and A. E. Rodrigues, Insight into steam reforming of ethanol to produce hydrogen for fuel cells, *Chem. Eng. J.*, 2006, **117**, 39–49, DOI: **10.1016/j.cej.2005.12.008**.

48 M. Konsolakis, Z. Ioakimidis, T. Kraia and G. Marnellos, Hydrogen Production by Ethanol Steam Reforming (ESR) over CeO2 Supported Transition Metal (Fe, Co, Ni, Cu) Catalysts: Insight into the Structure-Activity Relationship, *Catalysts*, 2016, **6**, 39, DOI: **10.3390/catal6030039**.

49 A. E. Shilov and G. B. Shul'pin, Activation of C−H Bonds by Metal Complexes, *Chem. Rev.*, 1997, **97**, 2879–2932, DOI: **10.1021/cr9411886**.

50 R. D. Shannon, Revised effective ionic radii and systematic studies of interatomic distances in halides and chalcogenides, *Acta Crystallogr., Sect. A*, 1976, **32**, 751–767, DOI: **10.1107/S0567739476001551**.

51 L. Vegard, Die Konstitution der Mischkristalle und die Raumfüllung der Atome, *Z. Phys.*, 1921, **5**, 17–26, DOI: **10.1007/BF01349680**.

52 N. Mota, I. Z. Ismagilov, E. V. Matus, V. V. Kuznetsov, M. A. Kerzhentsev, Z. R. Ismagilov, R. M. Navarro and J. L. G. Fierro, Hydrogen production by autothermal reforming of methane over lanthanum chromites modified with Ru and Sr, *Int. J. Hydrogen Energy*, 2016, **41**, 19373–19381, DOI: **10.1016/j.ijhydene.2016.05.029**.

53 M. Coskun, O. Polat, F. M. Coskun, Z. Durmus, M. Caglar and A. Turut, Synthesis, characterization and wide range frequency and temperature dependent electrical modulus study of LaCrO3 and cobalt (Co) doped LaCrO3 perovskite compounds, *Mater. Sci. Eng., B*, 2019, **248**, 114410, DOI: **10.1016/j.mseb.2019.114410**.

54 M. Marasi, L. Duranti, I. Luisetto, E. Fabbri, S. Licoccia and E. Di Bartolomeo, Ru-doped lanthanum ferrite as a stable and versatile electrode for reversible symmetric solid oxide cells (r-SSOCs), *J. Power Sources*, 2023, **555**, 232399, DOI: **10.1016/j.jpowsour.2022.232399**.

55 D. J. Morgan, Resolving ruthenium: XPS studies of common ruthenium materials, *Surf. Interface Anal.*, 2015, **47**, 1072–1079, DOI: **10.1002/sia.5852**.

56 M. Krumpelt, C. Rossignol and D.-J. Liu, Catalysis by Single Ions in a Host Lattice, *Catal. Lett.*, 2008, **124**, 13–17, DOI: **10.1007/s10562-008-9520-7**.

57 C. E. García-Vargas, X. I. Pereira-Hernández, D. Jiang, R. Alcala, A. T. DeLaRiva, A. Datye and Y. Wang, Highly Active and Stable Single Atom Rh1/CeO2 Catalyst for CO Oxidation during Redox Cycling, *ChemCatChem*, 2023, **15**, e202201210, DOI: **10.1002/cctc.202201210**.

58 W. Kobsiriphat, B. D. Madsen, Y. Wang, L. D. Marks and S. A. Barnett, La0.8Sr0.2Cr1−xRuxO3−δ–Gd0.1Ce0.9O1.95 solid oxide fuel cell anodes: Ru precipitation and electrochemical performance, *Solid State Ionics*, 2009, **180**, 257–264, DOI: **10.1016/j.ssi.2008.12.022**.

Supplementary Information

Enhanced ethanol reforming with catalytic active ruthenium species derived from solid solution in lanthanum chromite

Tamara S. Moraes[a]*; Victor B. Tinti[b,c]*, Fernando Piazzolla[a], Daniel Z. de Florio[b], Andre S. Ferlauto[b], Yohei Miura[d], David P. Dean[e], Jeffrey T. Miller[e], Abhaya K. Datye[f], Hien N. Pham[f], Fabio C. Fonseca[a†]

[a]Nuclear and Energy Research Institute, IPEN-CNEN, São Paulo, 05508-000, Brazil.

[b]Center for Engineering, Modeling and Applied Social Sciences, Federal University of ABC, Santo André 09210-580, SP, Brazil.

[c]Department of Energy Conversion and Storage, Technical University of Denmark, 2800 Kgs. Lyngby, Denmark.

[d]Nissan Research Centre, Nissan Motor Corporation Limited, Kanagawa, 237-8523, Japan.

[e]Davidson School of Chemical Engineering, Purdue University, 480 Stadium Mall Drive, West Lafayette, IN 47907-2100, USA.

[f]Department of Chemical & Biological Engineering and Center for Micro Engineered Materials, University of New Mexico, Albuquerque, NM, 87131, USA.

*These authors contributed equally to the work.

[†]Corresponding Author: fabiocf@usp.br

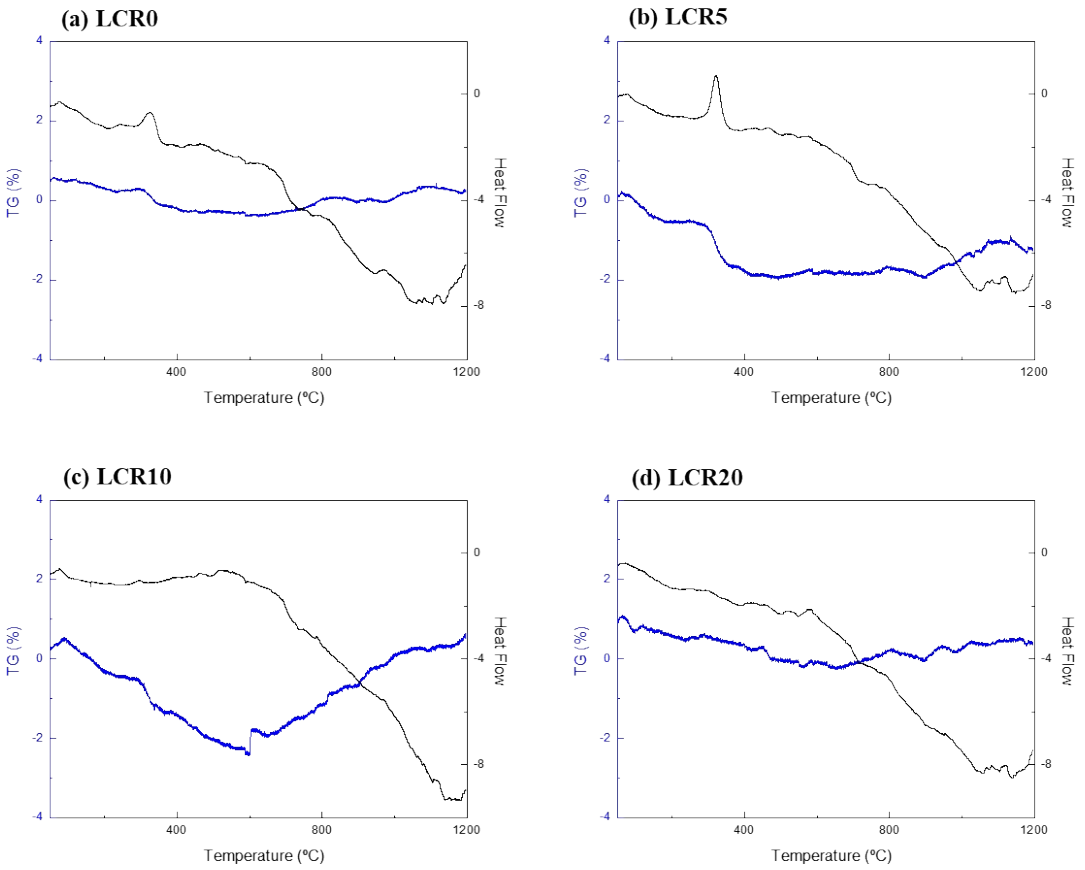

Figure S1. TGA/DTA measurements of the (a) LCR0, (b) LCR5, (c) LCR10, and (d)LCR20 after ESR measurements.

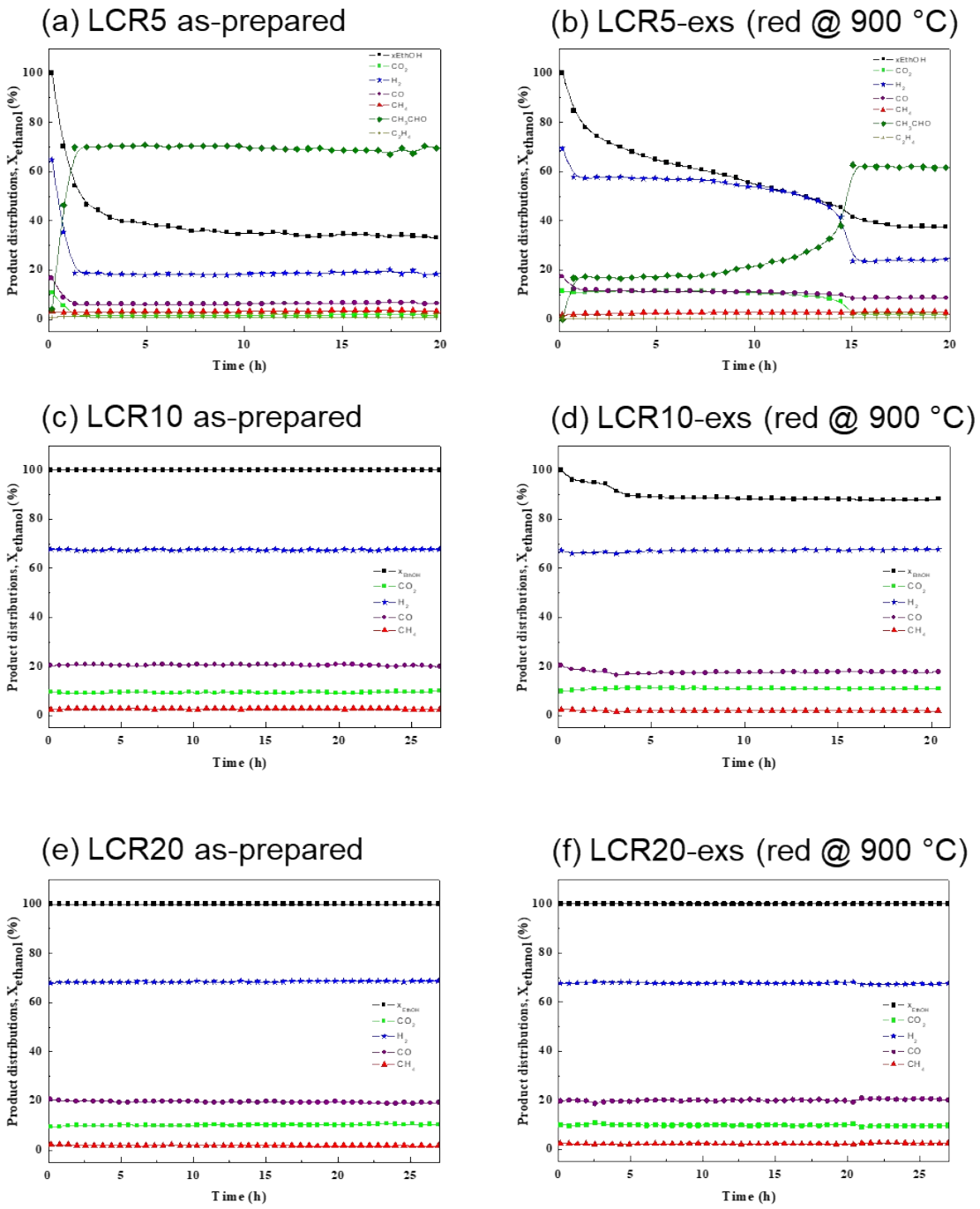

Figure S2. Ethanol conversion over time. Ethanol conversion (□, Xethanol) and product distributions versus TOS for ESR at 600 °C under H2O/ethanol molar ratio = 3.0. (left) Calcined (as-prepared) and (right) pre-reduced (900 °C/6 h in H_2) (a-b) LCR5, (c-d) LCR10, and (e-f) LCR20 samples.

Fig. S2 compares the ESR catalytic tests of samples as-prepared (LCR) and samples exsolved at 900 °C (LCR-exs). The LCR5 catalyst showed the formation of H2, CO, and CO2 during the first 2 hours of TOS (Fig. S2) indicating that ESR and WGS reactions occur. However, after 2 hours, the catalyst activity decreases leading to a shift in selectivity toward the formation of acetaldehyde and H2. After the exsolution treatment, the LCR5-exs sample activates for

ESR, reaching total conversion at the beginning of the measurement despite the relative low concentration of Ru, evidencing the active role of Ru0 for the ESR. However, the material quickly deactivates, with a major loss of performance after 15 hours of operation, switching the main reaction from ESR to ethanol dehydrogenation.

Increasing the Ru doping resulted in active LCRx ($x \geq 0.10$) samples. The LCR10 showed excellent ESR performance, with 100% ethanol conversion and no indication of deactivation after 20 hours of TOS. The LCR10-exs catalyst exhibited an initial conversion of 100%, with the same product distribution as LCR10. However, the LCR10-exs, surprisingly, rapidly deactivated and stabilized at ~90% conversion for TOS > 3 hours. Such a result indicated that exsolution treatment decreased the catalyst performance of the LCR10.

Regardless of the reduction thermal treatment, both LCR20 samples kept a 100% ethanol conversion rate without any deactivation during the 20-hour TOS. The short-term stability of the LCR20 samples is attributed to the larger Ru concentration, as compared to the LCR10 sample, which mitigates the deactivation despite the possibly larger particle size of the Ru after the exsolution reducing treatment.

Figure S3 illustrates the conversion rate and product distribution for 200 hours of ESR reaction at 600 °C and 700 °C for the LCR20-exs catalyst in the same conditions of **Fig. 2**. At 600 °C the LCR20-exs shows a faster deactivation (after ~30 hours of operation) as compared to the LCR20 as-prepared shown in **Fig. 2**. At 700 °C, the LCR20-exs sample remained stable during 200 hours of reaction, producing only H_2, CO, and CO_2. The observed stepwise deactivation curve may reflect a characteristic behavior of the material and reaction conditions in which catalytic activity declines in successive drops interspersed with periods of apparent stability. The stability plateaus can indicate intervals when carbon accumulation on the catalyst surface is partially balanced by its removal, promoted by the presence of steam. Additionally, this behavior may be associated with a transition in the reaction regime, shifting from predominantly kinetic control to internal diffusion control, because of progressive carbon buildup or pore blockage.

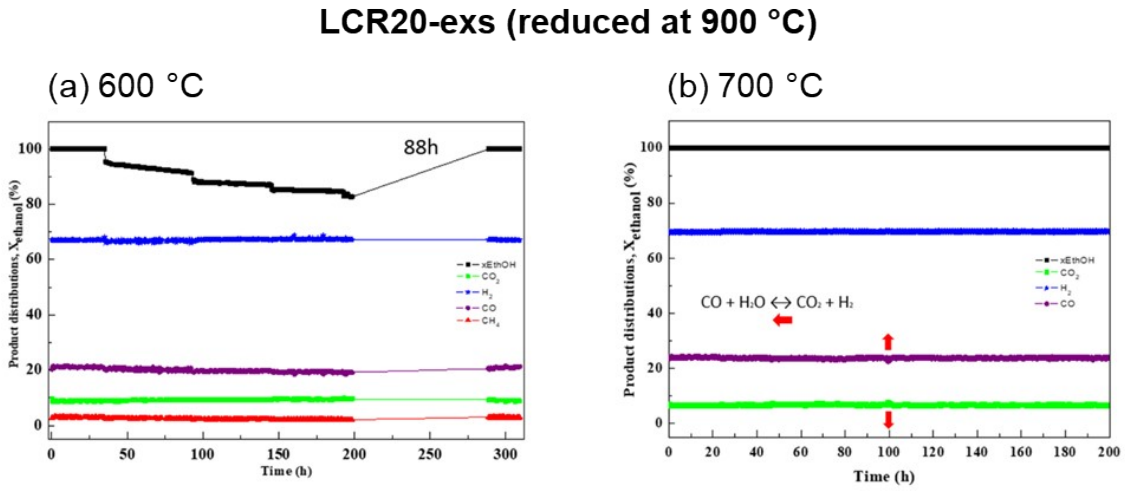

Figure S3. Ethanol conversion (□, Xethanol) and product distribution versus TOS for ESR over LCR20-exs at (a) 600 °C (same as in Fig. 2) and (b) 700 °C under H_2O/ethanol molar ratio = 3.0 (Mass of catalyst = 20 mg and residence time = 0.020 g s/mL).

Figure S4 illustrates the influence of steam concentration in ethanol reform deactivation. The increase in steam ratio resulted in a slower deactivation, at least initially. However, it also induced the flip from ethanol reform to dehydrogenation earlier, only after 5 hours of operation. Therefore, the steam can be used initially to prevent the loss in performance, but it also participates in the deactivation process.

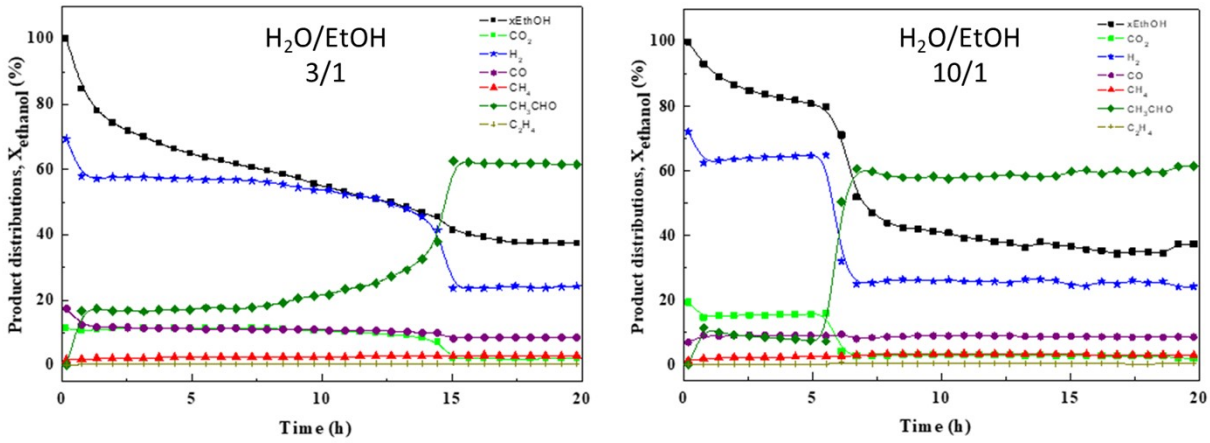

Figure S4. Adding excess water to ESR was ineffective for preventing LCR5-exs sample deactivation.

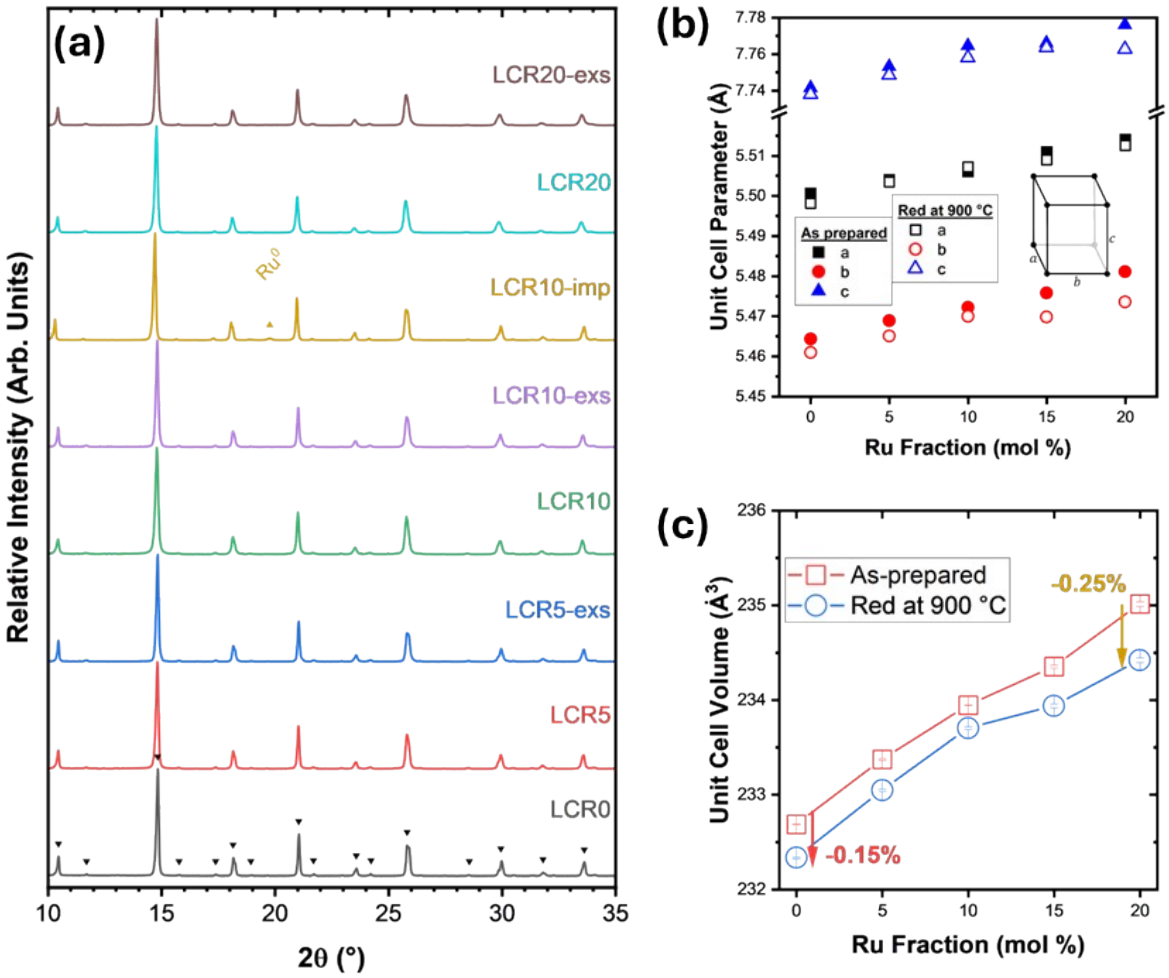

Figure S5. (a) XRD patterns for the as-prepared powders and after reduction treatment at 900 °C (exs). (b) Unit cell parameters dependence on the Ru content for as-prepared (closed symbols) and reduced at 900°C in H_2 (open symbols). (c) Unit cell volume calculated from XRD using Rietveld refinement. Lines connecting points are a guide to the eyes.

Table S1. Calculated results and parameters by Rietveld Refinement from the XRD patterns.

	As prepared			
	LCR0	**LCR5**	**LCR10**	**LCR20**
R_{wp}	8.0383	8.0512	8.2880	8.2063
a (Å)	5.5006	5.5040	5.5060	5.5140
b (Å)	5.4643	5.4688	5.4721	5.4811
c (Å)	7.7416	7.7531	7.7646	7.7760
Volume ($Å^3$)	232.68	233.37	233.94	235.01
Crystallite (nm)	128.73	158.46	123.76	258.96
Strain	0.2193	0.2895	0.2950	0.5458
B_{Ru} Occupation		0.06295	0.1129	0.1754

Table S2. EDS measurements for LCR samples.

Sample #		1	2	3	4	5	Mean	Std Dev
LCR00	La	51.22	51.00	51.19	51.23	51.25	51.18	0.10
	Cr	48.78	49.00	48.81	48.77	48.75	48.82	0.10
	Cr/La	0.95	0.96	0.95	0.95	0.95	0.95	-
LCR05	La	51.45	51.46	51.71	51.67	51.89	51.64	0.18
	Cr	46.33	46.42	45.74	45.52	45.58	45.92	0.43
	Ru	2.22	2.12	2.55	2.81	2.53	2.45	0.28
	Cr/La	0.90	0.90	0.88	0.88	0.88	0.89	0.01
	Ru/La	0.04	0.04	0.05	0.05	0.05	0.05	0.01
LCR10	La	51.54	51.74	51.38	51.70	51.88	51.65	0.19
	Cr	44.26	44.01	43.36	43.65	42.55	43.57	0.66
	Ru	4.20	4.25	5.26	4.65	5.57	4.79	0.61
	Cr/La	0.86	0.85	0.84	0.84	0.82	0.84	0.01
	Ru/La	0.08	0.08	0.10	0.09	0.11	0.09	0.01
LCR20	La	51.52	51.87	51.77	51.58	51.50	51.65	0.16
	Cr	40.58	39.61	39.41	38.64	37.94	39.24	1.00
	Ru	7.90	8.52	8.82	9.78	10.56	9.12	1.05
	Cr/La	0.79	0.76	0.76	0.75	0.74	0.76	0.02
	Ru/La	0.15	0.16	0.17	0.19	0.21	0.18	0.02

Table S3. Hydrogen consumption (μmolH2/g_{cat}) by region for samples as-prepared (LCRx) and ex-situ reduction in H_2 at 900 °C samples (LCRx-exs).

Region	Hydrogen consumption (μmol H_2/g_{cat})							
	LCRx				LCR-imp	LCRx-exs		
	0	5	10	20		5	10	20
I	-	-	-	-	-	0.61	3.37	3.01
II	5.91	5.48	8.68	6.84	95.35	8.90	20.09	20.01
III	13.62	8.20	14.65	20.10	-	-	-	-
IV	-	2.30	3.69	4.26	-	-	-	-
V	4.06	3.49	8.46	8.58	3.07	-	-	-

After ex-situ reduction at 900 °C (LCRx-exs) in H_2 (Table S3), the TPR profiles of the Ru-doped samples showed significant hydrogen uptake in region II (up to 20.09 μmol H_2/g_cat), and the emergence of reduction in region I, indicating increased surface accessibility and enhanced redox dynamics of metallic Ru^0 species. Overall, TPR analyses suggested that Ru doping creates a more versatile and active redox system, which may enhance catalytic performance in reforming reactions.

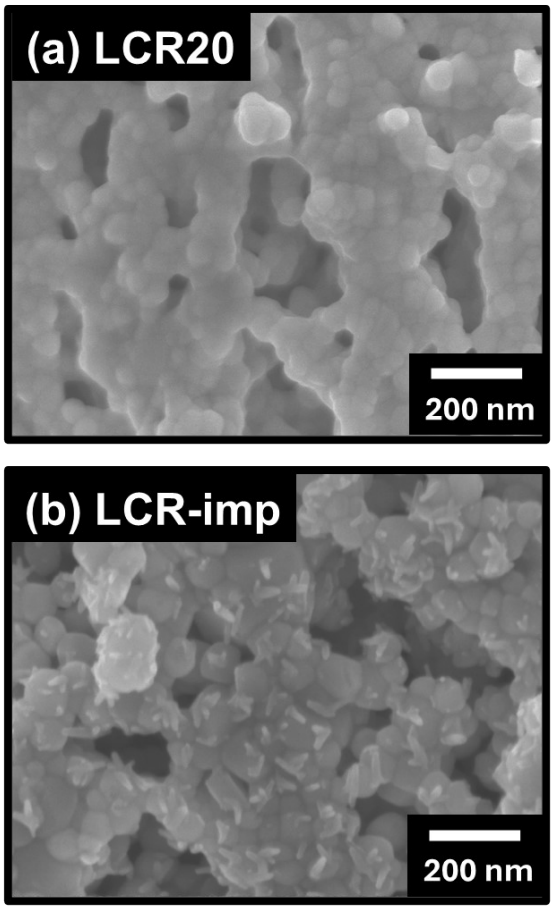

Figure S6. SEM image of the (a) LCR20 and (b) LCR-imp as-prepared.

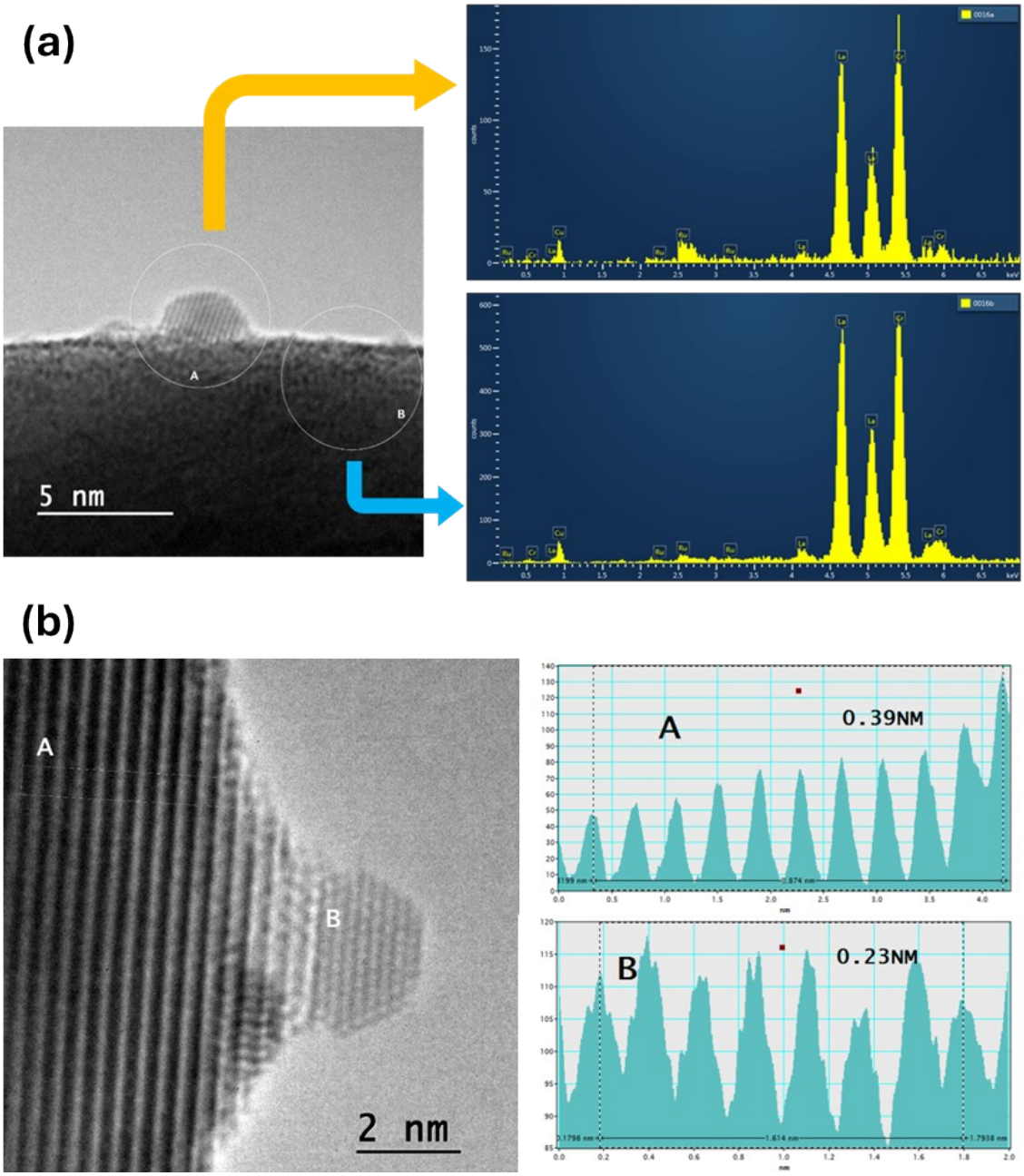

Figure S7. (a) HR-TEM image of the LCR20-exs and the corresponding EDS maps of regions A and B. Higher ruthenium counting are observed in the spot region A in which a large exsolved nanoparticle is observed. (b) HR-TEM image of the LCR20-exs and the corresponding diffraction patterns for regions marked as A ($LaCrO_3$) and B (Ru), with the corresponding fast Fourier transforms and calculated distances calculated to represent $LaCrO_3$ [020] and Ru [100].

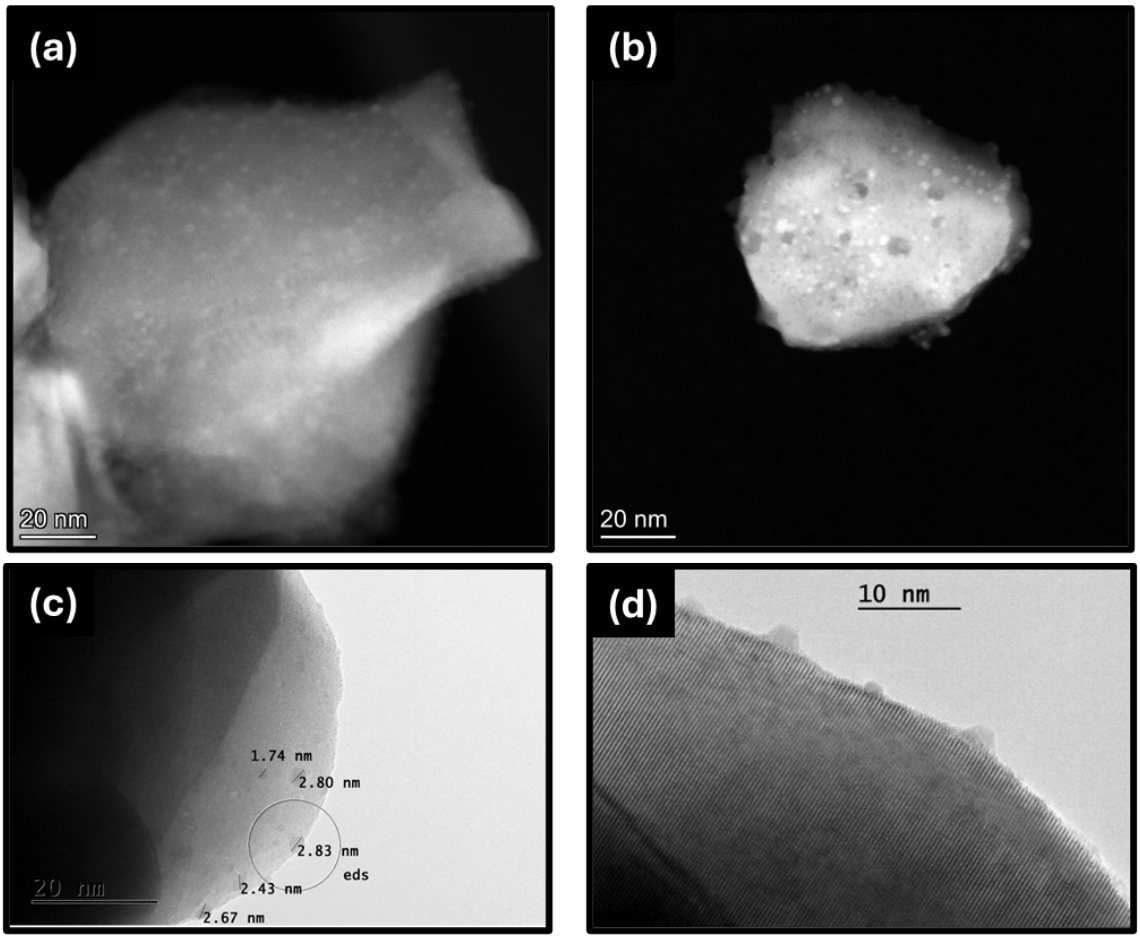

Figure S8. (a, b) HAADF-TEM and (c, d) HR-TEM images of LCR-20 after reduction at 900 °C, showing different regions of the sample.

When exposed to the reducing treatment. the Ru binding energy in the LCR-exs samples showed that the Ru4+Δ is effectively reduced to a lower valence state approaching the metallic ruthenium. but still slightly higher than the value reported for Ru0 (461.3 eV). However. only part of Ru is exsolved during the reduction treatment and a considerable amount of ruthenium remains in the bulk of the solid solution. Such a surface reduction is in accordance with the TPR data and suggests that Ru4+Δ surface species are susceptible to reduction at low temperatures and are the precursor of metallic ruthenium species.

Previous simulations of the exsolution mechanism showed a limited depth for the nucleation and growth of exsolved nanoparticles. estimated to be a few nanometers under the oxide surface. Coincidently XPS is probing the surface states that undergo exsolution. which correspond to the defective surface of the perovskite rather than the bulk ionic state of the metal cations in the ceramic oxide. Therefore. as an initial picture of the system. it is possible to assume that the high valence ionic states of both Ru and Cr close to the surface are the ones more prone to reduce and exsolve. Such species can result from exposed perovskite BO6-δ terminations with (Cr. Ru)+ΔO6-δ octahedra. Moreover. it is important to consider that XPS data can be misleading for such nanostructured powder materials that are likely to have adsorbed species. e.g.. H2O and CO2. in contact with the ambient atmosphere. which imposes difficulties on the XPS data analysis.

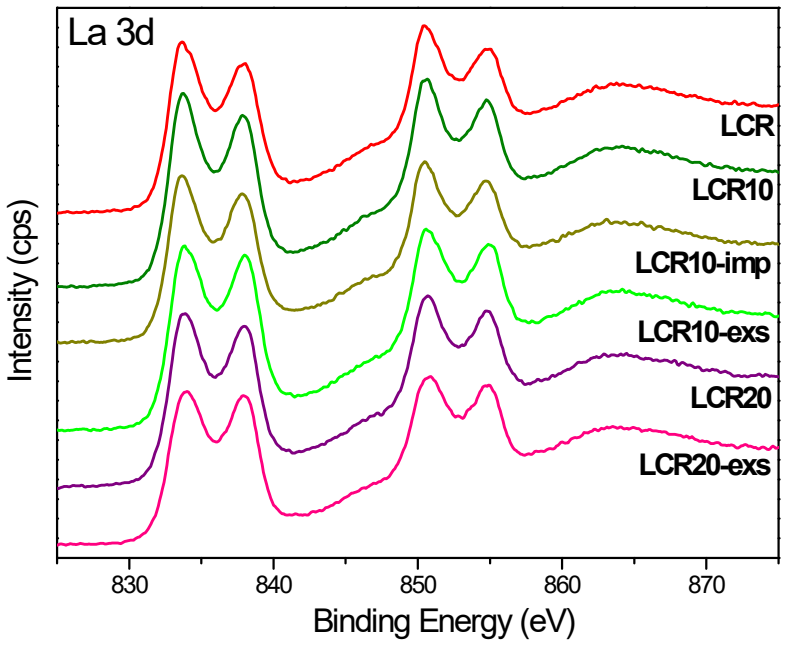

Figure S9. XPS peaks referring to lanthanum (La3d3/2. and La3d5/2).

Table S4. XAS experiments results.

Sample	Treatment	XANES Energy. keV	Fraction Ru+4	Fraction Ru^0	Scatter	CN	R	$\Delta\sigma^2$ ($x10^3$)	Eo. eV
Ru Foil	Ref	22.1170	-	100	Ru-Ru	12	2.68	0.0	-0.5
RuO_2	Ref	22.1292	100	-	Ru-O	6	1.98	8.0	-1.5
Ru/SiO_2	Reduction 550°C	22.1170	-	100	Ru-Ru	11.4	2.68	0.0	-1.8
Ru/SiO_2	Reduction 550°C. O_2 RT	22.1170	-	100	Ru-Ru	11.3	2.67	0.0	-2.0
LCRu20	Cal 1000°C as prepared	22.1288	100	-	Ru-O	5.9	2.01	2.0	2.5
LCRu20	Cal 1000°C As prepared + Reduction 550°C	22.1270	95	5	Ru-O	5.7	2.04	2.0	1.7
					Ru-Ru	-	-	-	-
LCRu20-exs	Red 900°C as received	22.1168	70	30	Ru-O	4.2	2.04	2.0	9.9
					Ru-Ru	2.0	2.64	2.0	-1.7
LCRu20-exs	Red 900°C. + Reduction 550°C	22.1170	60	40	Ru-O	3.7	2.04	2.0	9.2
					Ru-Ru	2.7	2.64	2.0	-0.5
LCR10-imp	as prepared	22.1286	100	-	Ru-O	5.9	1.97	2.0	1.3
LCR10-imp	as prepared. + Reduction 550°C	22.1172	-	100	Ru-Ru	10.9	2.67	0.5	-0.4
LCR10-imp	as prepared. + Reduction 550°C. O_2 RT	22.1172	-	100	Ru-Ru	10.7	2.67	0.5	-1.1
LCRu10	Cal 1000°C as prepared	22.1284	100	-	Ru-O	6.1	2.01	2.0	2.1
LCRu10	Cal 1000°C as prepared + Reduction 550°C	22.1272	95	5	Ru-O	5.9	2.04	2.0	2.0
LCRu10-exs	Red 900°C as received	22.1271	85	15	Ru-O	5.1	2.04	2.0	2.7
LCRu10-exs	Red 900°C. + Reduction 550°C	22.1272	85	15	Ru-O	5.0	2.05	2.0	2.4
LCRu5	Cal 1000°C as prepared	22.1282	100	-	Ru-O	6.0	2.01	2.0	2.2
LCRu5	Cal 1000°C as prepared + Reduction 550°C	22.1272	100	-	Ru-O	6.2	2.03	2.0	2.2
LCRu5-exs	Red 900°C as received	22.1269	85	15	Ru-O	5.2	2.04	2.0	2.2
LCRu5-exs	Red 900°C. + Reduction 550°C	22.1171	85	15	Ru-O	5.1	2.04	2.0	2.2

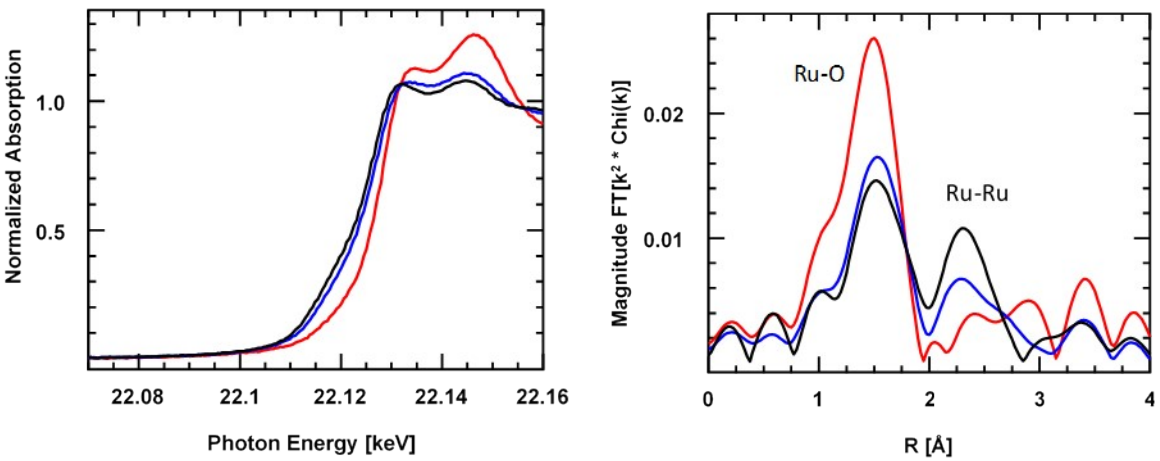

Figure S10. The Ru K-edge XANES of LCR20 calcined **(Red).** LCR20-exs (reduced at 900 °C and exposed to air at RT) **(Black)** and LCR20-exs (and reduced at 550 °C) **(Blue)**. XANES spectra from 22.07 to 22.16 keV and the k^2-weighted magnitude of the Fourier transforms from k = 2.5 –11.0 $Å^{-1}$.

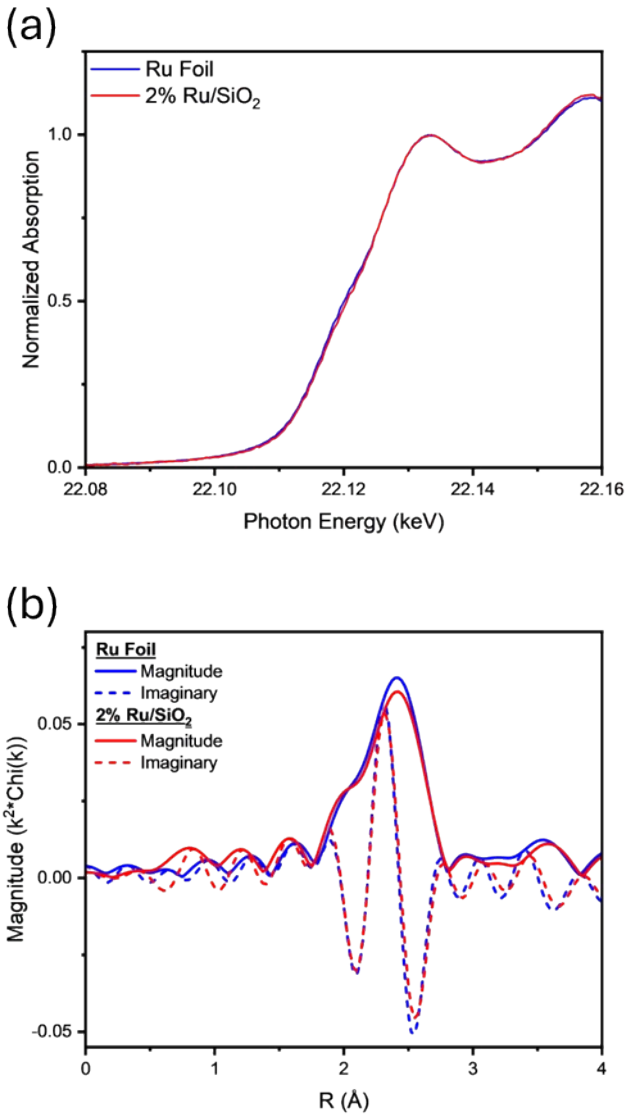

Figure S11. (a) XANES and (b) FTT for the Ru foil standard and 2% (wt.) Ru/SiO_2 reference catalyst.